Evidence of Pre-formed Lewis Acid-Base and Wheland-Type Complexes Acting as Dopants for *p*-Type Conjugated Polymers

Tushita Mukhopadhyaya[1], Taein Lee[1], Connor Ganley[2], Paulette Clancy[2] and Howard E. Katz[1,3]*

[1]Department of Materials Science and Engineering, Johns Hopkins University, 206 Maryland Hall, 3400 North Charles Street, Baltimore, MD 21218

[2]Department of Chemical and Biomolecular Engineering, Johns Hopkins University, 3400 North Charles Street, Baltimore, MD 21218

[3]Department of Chemistry, Johns Hopkins University, 3400 North Charles Street, Baltimore, MD 21218

*corresponding author, email hekatz@jhu.edu

Abstract

Efficient doping of polymer semiconductors is essential for their development as conductors. Although Lewis acids such as $B(C_6F_5)_3$ have shown promise as dopants for polymers, their doping mechanism is not fully understood. We created 1:1 zwitterionic (including "Wheland-type") complexes of $B(C_6F_5)_3$ with conjugated molecules difluoro bis(triethylsilylethynyl) anthradithiophene (diF-TES-ADT) and didodecylthienothiophene (DTT-12) and characterized them with ^1H NMR, UV-visible spectroscopy, EPR spectroscopy, optical and scanning electron microscopy-energy-dispersive x-ray spectroscopy (SEM-EDS), and x-ray diffraction. We employed these complexes as *p*-dopants for three conjugated polymers and established their doping abilities by conductivity measurements, Seebeck studies, field effect transistor (FET), and remote-gate sensing (RG-FET) measurements. Conductivity changes were dependent on the conjugated molecule adduct component, consistent with the adduct itself serving as the oxidant. The adduct complexes were capable of inducing changes in the surface potential of spun polymer films similar to the behavior shown by conventional dopants. Charge carrier density calculations by remote gate sensing revealed that these adducts can generate holes. We also studied the effect of adding the $B(C_6F_5)_3$ first, followed by addition of the neat conjugated molecules; the observation of behavior that was different from that using preformed adducts was consistent with the adducts remaining intact during doping. When $B(C_6F_5)_3$ was added to the polymers, followed by uncomplexed conjugated molecules, the generated hole carrier density is lower than that generated by the $B(C_6F_5)_3$ dopant but often greater than that generated by the Wheland complexes, indicating a high probability adduct formation in this case. Density functional theory calculations show that adduct formation between boranes and the conjugated molecules and segments of the polymers is energetically favorable, and that some charge transfer between adducts and neutral polymers is plausible if Coulombic and entropic effects are taken into consideration. Thus, such adducts can be considered as possible doping sites for conjugated polymers.

Keywords: *Wheland complexes*, *polymer adducts*, *direct doping*, *Lewis-acid dopants*, *doping mechanism, remote-gate sensing*

1. Introduction

Conjugated polymers possess several attractive properties such as being lightweight, solution-processable, and mechanically flexible, making them promising as charge injection layers for optoelectronic devices, films for electronic shielding, chemical sensing layers, and wearable electronics. Molecular doping has been shown to be effective for increasing the electrical conductivities (σ) of semiconducting polymers for a variety of applications such as organic thermoelectrics.[1] During this process, an integer electron transfer occurs as a result of an energetically favorable redox reaction between a π-conjugated polymer and the dopant resulting in a donor–acceptor association.[2] There have been several recent approaches in the literature in terms of dopant and/or polymer backbone and side-chain design, dopant volume, optimization of thin-film morphology and novel-device architectures[3] to achieve high conductivity from heavily doped conjugated polymers.[4] Despite such accomplishments in the optimization of conjugated polymers and dopants, high doping-induced conductivities have been achieved only to a limited extent in semicrystalline, polymeric semiconductors because of confinement of the donor–acceptor interactions to regions of intercalation of dopants within free-volume created by side-chains.[5]

A recent application of conductive polymers is flexible thermoelectrics. The most relevant thermoelectric parameter is known as the power factor (PF),[6] which can be calculated from the following equation $PF = S^2\sigma$ where S is the Seebeck coefficient (μV K^{-1}) and the conductivity, σ, is in S cm^{-1}. There is a trade-off between Seebeck coefficient and electrical conductivity (σ) because doping leads to higher carrier concentration, thereby boosting conductivity while simultaneously reducing the difference between Fermi and transport levels and thus the Seebeck coefficient. An optimal balance between conductivity and Seebeck coefficient maximixes the power factor, which, in turn, controls the thermoelectric conversion for useful power extraction.[7] The concentration of charge carriers (ρ) strongly governs σ and S and hence PF.[8] Optimizing PF is quite challenging[9] because each of its two factors has a complicated and contrary dependence on the carrier concentration.[10] σ for the most conductive p-type polymers is on the order of hundreds to thousands of S cm^{-1}, and PF is usually tens to hundreds of μW m^{-1} K^{-2}. More fundamentally, this contrary dependence provides an additional indication of doping activity and additional insight into the energy distribution of doping-induced charge carriers.

Doping organic semiconductors was first accomplished using small molecule oxidants such as AsF_5, Br_2, and I_2 vapors, which drastically improved σ to ~10 S cm^{-1}. Metal atom-centered dopants like SbF_5 and $FeCl_3$ gained popularity as they are non-volatile, allowing for constant doping levels over time.[11] Although I_2,[12] $FeCl_3$,[13] and $SbCl_5$,[14] are strong dopants, they are rarely used in organic devices

due to their high sensitivity to air and corrosivity. Alternatively, electron-deficient organic *p*-dopants such as tetrafluorotetracyanoquinodimethane (F_4TCNQ),[15] its derivatives, and, more recently, 2,2-(perfluoronaphthalene-2,6-diylidene)dimalononitrile (F_6TCNNQ) have been widely used for the generation of highly conductive interlayers in organic electronic devices by virtue of their tunable electron affinity as well as device engineering using cascade strategies. It was demonstrated that doping of poly(3-hexylthiophene) (P3HT) and PBTTT by F_4TCNQ leads to a dramatic increase in the conductivity from 10^{-6} S cm^{-1} for neat polymers up to 1-2 S cm^{-1} for solution-processed doping and ~250 S cm^{-1} for the vacuum-deposited dopant.[16] Organic and inorganic salts of the hexacyano-[3]-radialene anion-radical have been employed for *p*-doping of P3HT to achieve high conductivities.[17] Lu *et al.* employed the trisaminomethane (TAM) derivative to achieve a high electronic (*n*-type) conductivity of ~20 S cm^{-1} at a relatively low doping level where TAM cations, by virtue of their small volume, facilitated the enhancement of mobility by doping. [18] Watanabe *et al.* have shown that doping efficiency of polymers with a sparse distribution of alkyl side-chains is significantly greater than that with dense side-chains, thereby emphasizing the importance of steric effects in the polymer.[19] Li *et al.* have designed polythiophenes incorporating sulfur or 3,4-ethylenedioxy groups on the side-chains to increase backbone oxidizability, density of binding sites for dopants, and the polymer's free volume, achieving a hole conductivity of ~330 S cm^{-1}.[20] Scholes *et al.* utilized a series of statistical copolymers of P3HT and poly(3-heptyl selenophene) for fine-tuning electronic structure and crystallinity to achieve highly mobile charge carriers in crystalline regions of the film.[21] Recently, a selenium-substituted *p*-type PDPPSe-12, on being doped with $FeCl_3$, achieved a record power factor ~364 μW m^{-1} K^{-2}.[22] Further, the sequential processing (SqP) method[23] has garnered increasing attention wherein a neutral polymer film is cast, followed by dopant deposition in a second casting step using an orthogonal solvent system, resulting in an undisturbed thin film morphology and optimum crystallinity control.

More recently, novel dopants based on organic salts have emerged to provide additional possibilities for doping procedures[24] beyond the neutral single-component molecular dopants mentioned above. Brønsted acids,[25] such as hydrogen fluoride and trifluoroacetic acid (TFA), were demonstrated to dope[26] by double protonation of a polymer chain, followed by an internal redox process to produce either bipolarons or singly charged polarons.[27] However, characterization of protonated intermediates and the resulting radical species have remained elusive. There is little knowledge about the species involved in such doping processes and the nature of the charge-transfer reactions.[28] Lewis acids are known to dope via Lewis acid-base adducts, driven by the interaction between the empty *p*-orbitals of the centrally electrophilic boron atom and the electron lone pair of a Lewis base (LB) site on the polymer, such as pyridyl nitrogen and pyridylthiadiazole (PT).[29]

There are many recent studies of the versatile *p*-doping capability of tris(pentafluorophenyl)borane ($B(C_6F_5)_3$ or BCF), due to its easy solution-processability and its interactions with polymers of high ionization potential (~5.8 eV),[30] besides its ability to modulate

polymer chain arrangements leading to a plethora of thin-film morphologies.[31,32] Mechanistic and theoretical studies[32] have revealed that BCF reacts with trace amounts of water present in the polymer to form a complex to release a proton that protonates the appropriate functionality in the conjugated polymer, which then becomes the new *in situ* dopant. Thus, these studies point towards the participation of BCF $(OH_2)_n$ adducts, *i.e.,* strong Bronsted acids which form under hygroscopic conditions, and not by a direct one-electron transfer.[32] For example, polymers like poly-cyclopentadithiophene-benzothiadiazole (PCPDTBT) can be doped by this mechanism. Anthopoulos *et al.* revealed the possibility of formation of adduct complexes involving $B(C_6F_5)_3$/ difluoro bis(triethylsilylethynyl) anthradithiophene (diF-TES-ADT) and $B(C_6F_5)_3$/bis(triisopropylsilylethynyl (TIPS)-pentacene and $Zn(C_6F_5)_3$/dioctylbenzothienobenzothiophene (C_8-BTBT) in polymer-conjugated molecule blends, but the direct experimental proof of the doping ability of the adducts was not established. [33] Han *et al*. demonstrated for the first time that a Meisenheimer addition complex of naphthalenediimide (NDI) with tetrabutylammonium fluoride (TBAF) could be used as a dopant to achieve electronic conductivity and high power factors in *n*-type polymers PNDICIVT and PBDOPVTT.[34,35] However, no analogous demonstration of the equivalent positively charged addition complex, sometimes termed a "Wheland intermediate" [35] (first considered as part of the electrophilic aromatic substitution mechanism) or Lewis basic atom complex functioning as a p-dopant has been reported, even though, if anything, it could be a more common species than the Meisenheimer complexes in doped polymers.[36,37]

In this paper, we have, for the first time, systematically investigated the ability of *pre-formed adducts* of the type $B(C_6F_5)_3$:"conjugated molecule" (where the conjugated molecule is diF-TES-ADT/didodecylthienothiophene, DTT-12) to serve as dopants for conductive polymers. We use the adducts to dope a series of three conjugated polymers (**Figure 1**) with different Lewis basicity, backbone functionality and nature of solid-state microstructure. Electrical measurements revealed that adducts are capable of generating hole carrier density of the same order of magnitude as that generated by $B(C_6F_5)_3$ alone, and can lead to a substantial power factor ~30$\mu VK^{-2}m^{-1}$. Subsequent investigation by UV-visible spectroscopy, microscopy, and SEM-EDS confirmed the doping phenomenon by revealing signatures of polaron evolution and aggregation morphology. We also fabricated control devices by adding the $B(C_6F_5)_3$ first, and then adding the conjugated molecules while maintaining the same concentration as $B(C_6F_5)_3$. This provides insight into whether an adduct is capable of being an independent doping entity, or if the adduct splits up, post-addition, into $B(C_6F_5)_3$ and the conjugated molecule, after which $B(C_6F_5)_3$ ends up being the actual dopant. Overall, our studies indicated, for the first time, that, while the adducts are less efficient than $B(C_6F_5)_3$ as dopants, they are *energetically favorable to form based on DFT calculations and chemical analyses, show clear dopant activity, and could be the active dopant species when Lewis acids are added to Lewis basic conjugated polymers.*

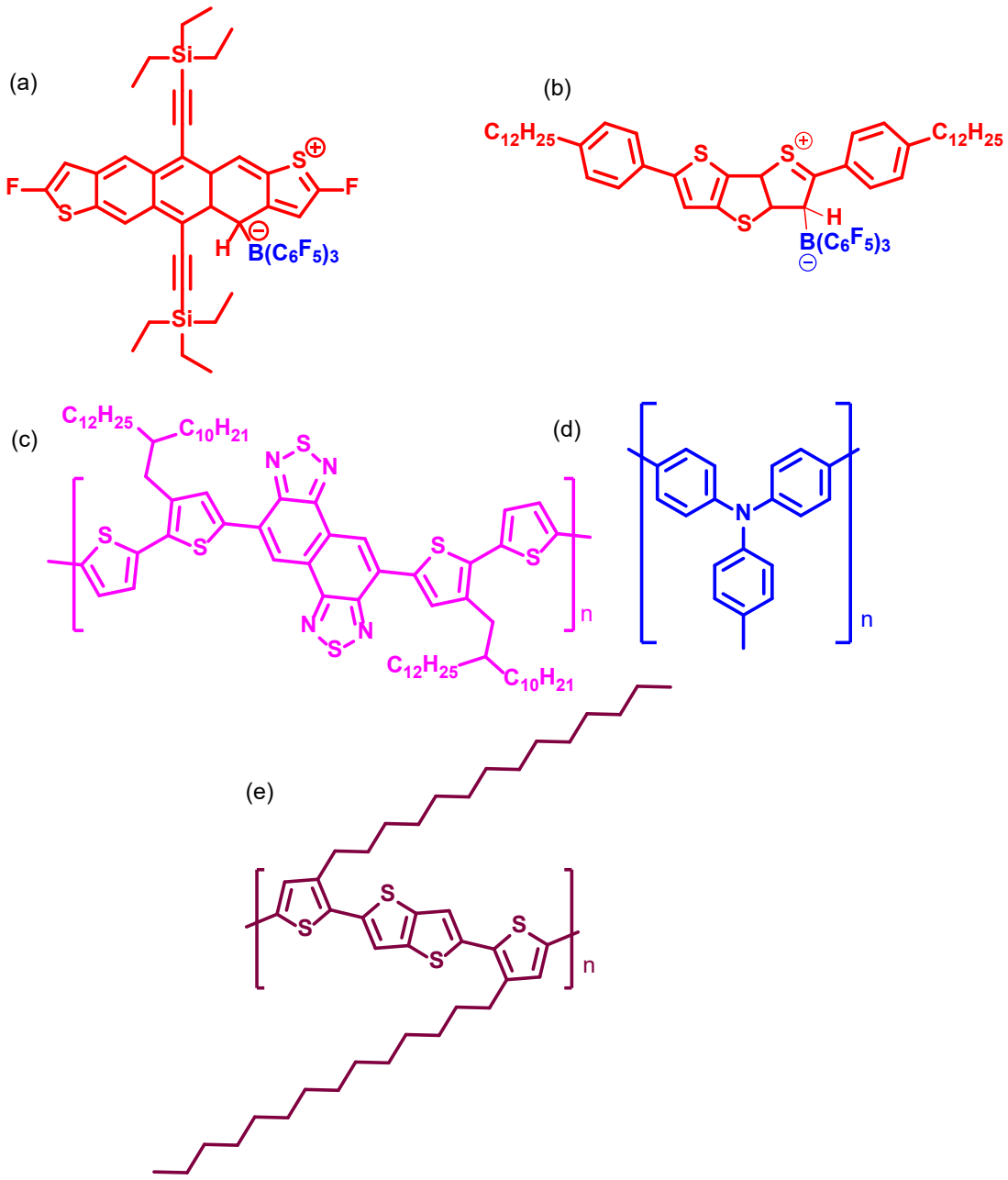

Figure 1. Adducts (a) $B(C_6F_5)_3$: diF-TES-ADT (b) $B(C_6F_5)_3$: DTT-12 and polymers (c) PNTz4T (d) PTAA and (e) PBTTT used in this study

We used the conjugated molecules diF-TES-ADT and DTT-12 to form Wheland-type or Lewis base adducts/complexes (**Figure 1**). The general structures of our Wheland complexes in **Figure 1** are based on *ab initio* geometry optimizations where the system was subjected to a large number of optimization cycles to arrive at a local energy minimum at a location above each respective polymer or small molecule in each of the simulations (details in the **SI**, computational section), with respect to the highly complex potential energy surface. The equilibrium structures thus generated are shown in **Figure S4, S5, SI** for $B(C_6F_5)_3$:diF-TES-ADT and $B(C_6F_5)_3$:DTT-12 with very similar bond enthalpies (**Table S2,**

S3, SI) which implies that multiple structures can co-exist. **Figure S6** and **Figure S7, SI** depicts the pi-interactions between the Lewis acid and our chosen conjugated small molecule (Lewis base). Anthopoulos *et al.* performed DFT calculations on adducts formed via B-C and B-N bonds in physisorbed and chemisorbed configurations, at the B3LYP/6-31G* level of theory using Gaussian 09 (total energy calculations were performed with the DFT code Quantum Espresso including van der Waals interactions within the DFT-D2 approach and exchange–correlation effects with the Perdew–Wang functional). These involved diF-TES-ADT and TIPS-pentacene. Their findings indicated a potential dual role of $B(C_6F_5)_3$ in affecting the long-range microstructure of the semiconducting layer along with binding at the molecular level to certain species of interest. However, they did not seem to identify stable adduct structures involving $B(C_6F_5)_3$ or quantify their contribution to chemical interactions and to the apparent *p*-doping.[33] Thus, we chose diF-TES-ADT as a suitable candidate to form the zwitterionic adducts. The DTT-12 conjugated molecule was also chosen as a means to study how changes in electronic/steric of the conjugated molecule affect its doping ability.[38] Both the conjugated molecules have been previously reported to be both highly crystalline and solution-processable. Throughout the text and figures the adducts have been referred to as $B(C_6F_5)_3$:diF-TES-ADT and $B(C_6F_5)_3$: DTT-12 respectively. The controls have been described as "$B(C_6F_5)_3$ followed by diF-TES-ADT/DTT-12 addition" throughout the text/figures. The electrical/structural/morphology characterization data of polymers have been designated as <polymer>_<dopant name> or <polymer>_<nature of the film> throughout the text.

2. Results and Discussions

2.1. Synthesis and Characterization of adducts

Conjugated molecule transfer curves and output characteristics are shown in **Figure S1, S2, SI** and the threshold voltage and mobility values are listed in **Table S1, SI**. Their high *p*-channel mobilities and positive threshold voltages indicate an electron-rich backbone, validating our choice of the conjugated molecules in promoting the thermodynamic and kinetic stability of the adduct complexes. Stock solutions of adducts $B(C_6F_5)_3$: diF-TES-ADT and DTT-12: $B(C_6F_5)_3$(mole ratio 1:1) were prepared by mixing the conjugated molecules diF-TES-ADT/DTT-12 and $B(C_6F_5)_3$ in a glove box (N_2, H_2O < 6 ppm, O_2 < 0.1 ppm) in anhydrous chlorobenzene (details in the Supporting Information). The color changes of the solutions as they undergo adduct formation are shown in **Figure S3, SI**. For diF-TES-ADT, the color of the solution changes from fluorescent orange to a wine-red while, for DTT-12, the color changes from yellow to red.

The ^{1}H NMR spectra of the conjugated molecules and their corresponding adducts are compared in **Figure S8-S13, SI**. From the ^{1}H NMR spectra of the neat conjugated molecules and their respective adducts it can be seen that: (a) The protons in the aromatic region become substantially deshielded

because of electron-deficiency in the semiconductor backbone as a consequence of complexion by the Lewis acid $B(C_6F_5)_3$. (b) From the ^1H NMR spectrum of diF-TES-ADT (**Figure S8, SI**), the peaks corresponding to the protons belonging to the benzene rings at δ 7.91-7.88 ppm are reduced in intensity and the apparent number of protons in the adduct ($B(C_6F_5)_3$:diF-TES-ADT) was reduced to half (**Figure S9, SI**). This indicates the involvement of either of them in the complexation process with $B(C_6F_5)_3$. It is also possible that $B(C_6F_5)_3$ coordinates with the C-C triple bond, such that the –R effect will cause the protons at δ 8.5-8.0 ppm to shift to the δ 8.0-7.5 ppm region. Two additional protons (**Figure S9, SI**) in the region δ 9.0-8.5 ppm also hint at the possibility of equilibrium with some uncomplexed diF-TES-ADT. However, the total number of protons in the aliphatic and aromatic regions remains the same, which indicates that the complexation partly occurs in the benzene region and also at the triple bond. (c) **Figure S10, S11, SI** illustrate ^1H NMR of DTT-12 and $B(C_6F_5)_3$:DTT-12, respectively. The ^1H NMR spectra of the aromatic regions are shown in **Figure S12, SI** (DTT-12) and **Figure S13, SI** ($B(C_6F_5)_3$: DTT-12). The protons are more deshielded due to an altered backbone electronic structure. The proton adjacent to the S atom corresponding to δ 7.41(s, 1H) disappears, as seen in **Figure S13, SI**. Our observations from ^1H NMR spectra correlate well and are in excellent agreement with the results of Density Functional Theory (**Figure S4-S7, SI**). We have also carried out characterizations of our Wheland complexes $B(C_6F_5)_3$:diF-TES-ADT and $B(C_6F_5)_3$:DTT-12 with electron paramagnetic resonance (EPR) spectroscopy (**Figure S14, SI**), which shows no evidence of free radicals in the Wheland complexes, meaning that these complexes must be via spin-paired dative bond and Lewis acid-base/ coordination interactions. **Figure 2** depicts the characterization of diF-TES-ADT and its corresponding $B(C_6F_5)_3$ adduct by X-ray diffraction (**Figure 2(a)**) and steady-state UV-visible spectroscopy carried out in solution (**Figure 2b**), and in the solid state (**Figure 2c**). The XRD and spectroscopic characterization for DTT-12 and its corresponding adduct $B(C_6F_5)_3$: DTT-12 are shown in **Figure S15, SI**. **Table S4, SI (a), (b)** summarises 2θ and 'd' value changes of the (*h00*) peak in the conjugated molecule diF-TES-ADT and DTT-12 as a result of this complexation process as per

Bragg's

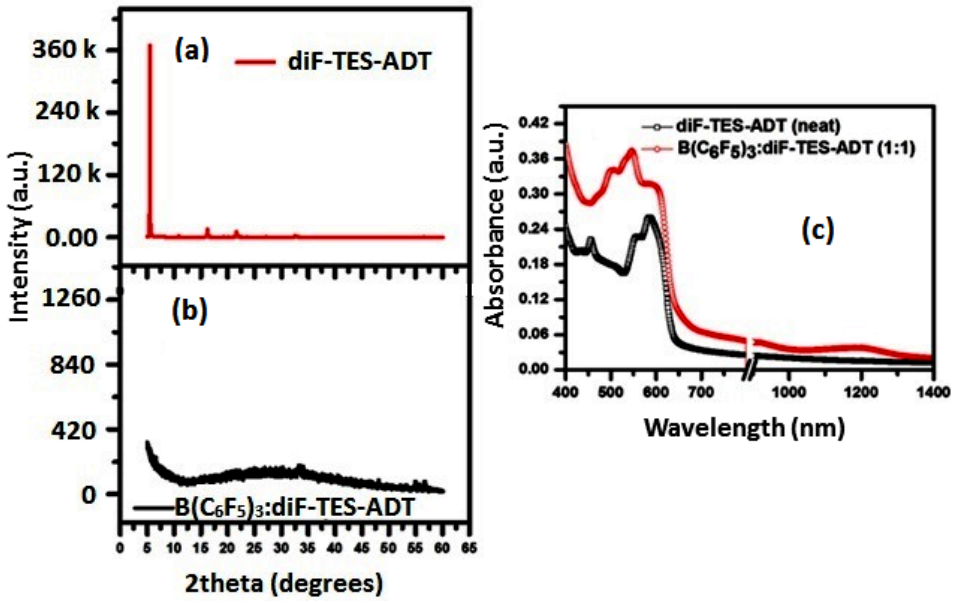

Figure 2. (a) X-Ray diffractograms of diF-TES-ADT and $B(C_6F_5)_3$: diF-TES-DT (b) UV-vis spectra of diF-TES-ADT and $B(C_6F_5)_3$: diF-TES-ADT in solution (c) UV-vis spectra of diF-TES-ADT and $B(C_6F_5)_3$:diF-TES-ADT in thin-film adduct $B(C_6F_5)_3$: diF-TES-ADT by thin-film XRD.

equation.[39] For diF-TES-ADT, it is observed that the crystallinity is lost due to the incorporation of $B(C_6F_5)_3$ in the matrix. $B(C_6F_5)_3$ occupies sites within lamellar stacks, forcing them apart. Although a similar loss of crystallinity of DTT-12, on reacting with the borane to form the adduct/Wheland complex, occurs by the similar mechanism as evidenced by ^{1}H NMR spectroscopy, UV-visible spectroscopy, and EPR spectra, it is not observable by X-ray diffraction in terms of change of peak positions. However, there is a slight decrease in peak intensities on comparing the top and lower panels of **Figure S15 (a), SI**. This indicates weak binding between the borane and DTT-12 with greater reversibility, as per the Hard-Soft-Acid-Base (HSAB) principle. The UV-visible spectrum (**Figure 2(b)** and **Figure S15, (b) and (c)**) shows the evolution of an additional peak at higher wavelength for both the conjugated molecules and a relative reduction in the intensity of the stronger absorption peak characteristic of the conjugated molecules.

We examined the microstructure of $B(C_6F_5)_3$ by X-ray diffraction and SEM-EDS. The small white coalesced aggregates resemble the microstructure typical of $B(C_6F_5)_3$ shown in **Figure S16, SI**. The neat $B(C_6F_5)_3$ film is devoid of crystal-like shapes and instead forms macrostructures with little definition. The thin film microscopy images (along with 3D height images) of diF-TES-ADT and DTT-12 are shown in **Figure S17 (a)**, **(b)** and **(c)**, **(d)**, respectively. DTT-12 exhibits flake-like structures with close packing, showing that it has a high driving force for crystallization. We performed SEM-EDS examination of diF-TES-ADT in its free and complexed forms (**Figure S18, SI**). We observed that the conjugated molecule forms well defined structures (corroborating the XRD study in **Figure 2**). **Figure 3** shows the morphology changes for diF-TES-ADT and DTT-12 on complexation with $B(C_6F_5)_3$. **Figure 3(a)** reveals that the crystalline appearance of diF-TES-ADT is lost in the adduct thin-

film. **Figure 3(b)** reveals the retention of the flaky nature of microstructures in the DTT-12 adduct thin film, compared to **Figure S17, SI**. This corroborates the minimal loss in crystallinity. **Table S5, SI** and **Table S6, SI** summarize the elemental composition analysis elucidated by SEM-EDS. **Table S6, SI** shows a low F content (%) and a high content (%) of S in the spots. Since $B(C_6F_5)_3$ itself is amorphous, these studies further confirm that the remaining or changed crystallinity in $B(C_6F_5)_3$-containing samples has a sole contribution from conjugated molecules.

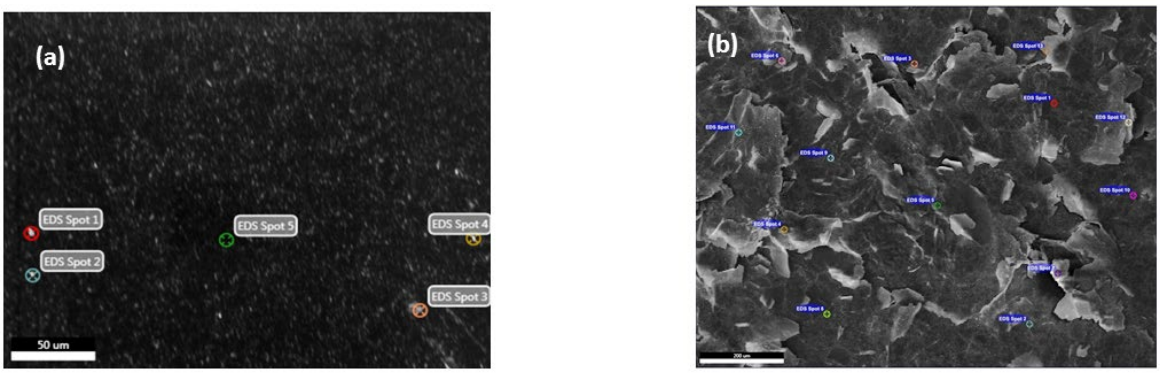

Figure 3. SEM images of (a) $B(C_6F_5)_3$: diF-TES-ADT (b) $B(C_6F_5)_3$: DTT-12

2.2. Electrical Characterization of Doped Polymers

2.2.1. Conductivity and thermoelectric studies

Having characterized the adducts $B(C_6F_5)_3$: diF-TES-ADT and $B(C_6F_5)_3$:DTT-12, we next investigated their capabilities to dope the polymers PNTz4T, PBTTT and PTAA[40,41] compared to their doping by $B(C_6F_5)_3$ alone. **Figure 4** shows the comparison and the trends in conductivity. The error bars represent uncertainty as a standard deviation. The value of σ was measured via a four-point probe method. The thin film preparation method is described in the SI. From our observations, we note that: [a] $B(C_6F_5)_3$ results in conductivities higher than those using the adducts, but of the same order of magnitude. [b] In the case of PNTz4T, the adduct $B(C_6F_5)_3$: DTT-12 gives rise to lower conductivities than $B(C_6F_5)_3$: diF-TES-ADT. The thickness of the films of all polymers employed in measurements of conductivity and Seebeck coefficients in this series are ~1.5-2.0 μm. A representative thickness profile of PBTTT is shown in **Figure S19, SI**.

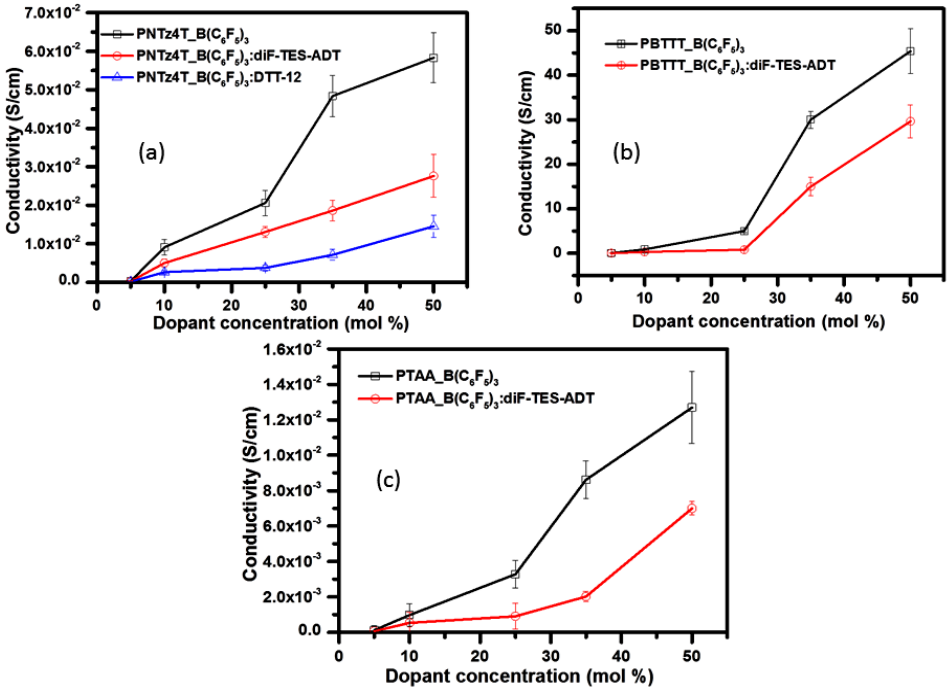

Figure 4. Variation of conductivity with dopant concentration on doping (a)PNTz4T with $B(C_6F_5)_3$, $B(C_6F_5)_3$:diF-TES-ADT and $B(C_6F_5)_3$:DTT-12 (b)PBTTT with $B(C_6F_5)_3$ and $B(C_6F_5)_3$:diF-TES-ADT and (c)PTAA with $B(C_6F_5)_3$ and $B(C_6F_5)_3$:diF-TES-ADT.

Figure S20, SI shows the conductivities of the controls which are sometimes different from adducts, but the trend is not consistent for every composition. As discussed earlier, control devices were fabricated by adding the $B(C_6F_5)_3$ first, and then adding the conjugated molecules while maintaining the same concentration as $B(C_6F_5)_3$ to obtain an insight into whether an adduct is capable of being an independent doping entity, or if the adduct splits up, post-addition, into $B(C_6F_5)_3$ and the conjugated molecule, after which $B(C_6F_5)_3$ ends up being the actual dopant. The moderate concentrations 20-35% may be more important. It may even be possible that the adduct forms in the control case, rather than the adduct separating in the non-control case. Also, it is possible that two types of dopants, $B(C_6F_5)_3$ and $B(C_6F_5)_3$:diF-TES-ADT both participate in the doping process in case of the controls, since the conductivity of the polymer films in the control cases (**Figure S20, SI**) seems to be a weighted average of the direct doping case and the adduct-doping case. *The highest conductivities that were achieved for the set of polymers used in this study were ~50 S cm^{-1} with $B(C_6F_5)_3$ and ~30 S cm^{-1} with $B(C_6F_5)_3$: diF-TES-ADT, for the same mol % of these two dopants, for PBTTT polymers.* The Seebeck Coefficient (S) was obtained by linear fitting of a data series taken by imposing temperature differences across the samples and measuring the thermo voltages. All the voltage versus temperature plots and the linear fitting to extract the value of S, are shown in **Figure S21-S25, SI**. In principle, S and σ are strongly and oppositely dependent on the carrier concentration associated with the electronic structure of the materials.[42] The trends in S of the polymers with change of dopant concentration ($B(C_6F_5)_3$ and the 2

adducts) are shown in **Figure 5** and in **Figure S26, SI** for the controls and are consistent with the established negative correlation with the charge carrier concentration. The S

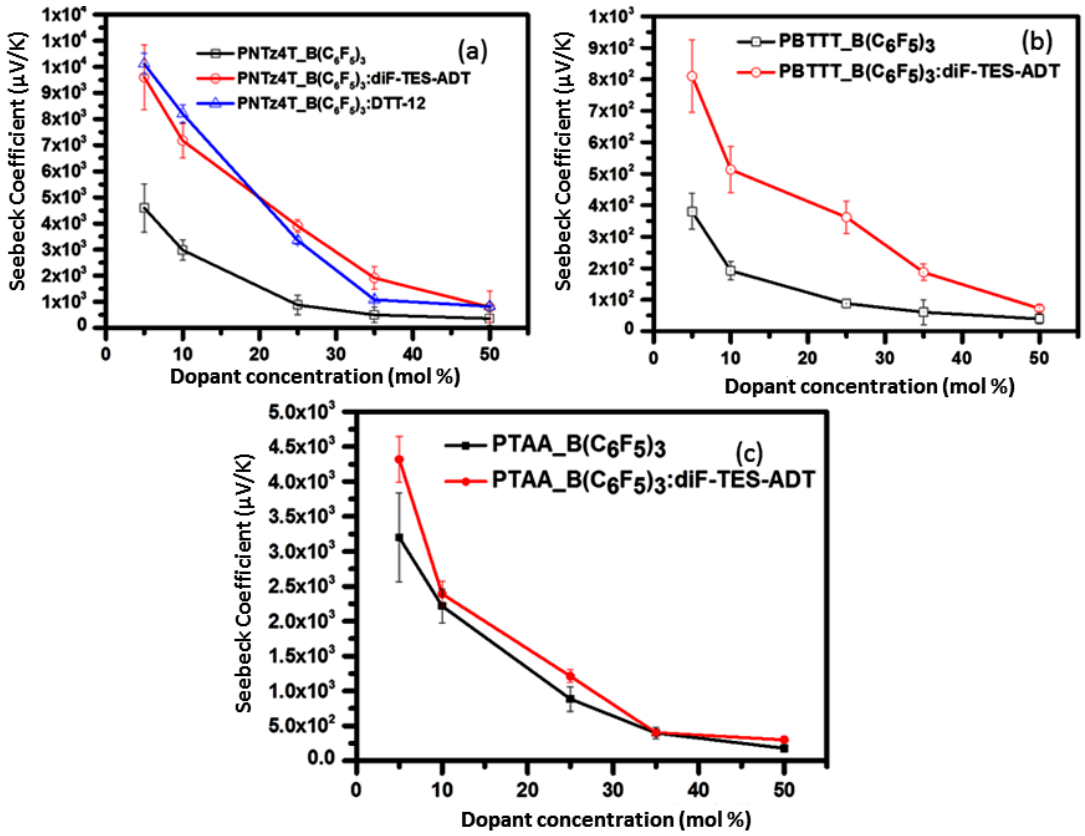

Figure 5. Seebeck coefficients of (a) PNTz4T (b) PBTTT and (c) with respect to dopant concentration (mol %).

values of the controls are shown in **Figure S26, SI**. Despite the individual dopants differing in their doping ability, **Figure S27, S28, SI** reveal that the fitting is consistent with S being a consequence of doping.[6] The power factors are collected in **Table 1** and those of controls are collected in **Table S7, SI**. For PNTz4T and PTAA, the power factors of the polymer are higher when doped with the adduct $B(C_6F_5)_3$: diF-TES-ADT/$B(C_6F_5)_3$: DTT-12. Surprisingly, for PBTTT and PTAA, power factors do not vary much with the nature of the dopant. The high power factor associated with adduct doping, despite the reduction of conductivity with increased dopant (adduct) concentration, could be associated with the creation of deeper energy states,[43,44] due to addition of the conjugated molecule or within aggregates that form more readily when the dopant is added in the adduct form. The SEM-EDS of the adducts $B(C_6F_5)_3$: diF-TES-ADT and $B(C_6F_5)_3$:DTT-12 (**Figure 3**) supports the increased tendency for aggregation as compared to the neat $B(C_6F_5)_3$ (**Figure S16, SI**) film. These aggregates would be present in addition to the presence of aggregates by the doped polymers. The additional holes formed on addition of larger mol % of dopants are first trapped in the deep states as movement of mobile charges to the shallow states is now difficult, due to incorporation of the conjugated molecule component of the dopant within polymer segments such that fewer charge carriers occupy shallow states.[45,46]We also

cannot rule out that the high Seebeck coefficient in adduct-doped polymers could be due to an ionic thermogalvanic effect (though we would not expect adducts to be more mobile than the separated ions), or an energy filtering contribution.[47] The Seebeck coefficients of the controls (**Figure S26, SI**) are different from those achieved by doping the polymers with the adducts. [48,49]

According to previous reports [50], σ follows an Arrhenius-type dependence of conductivity with temperature, *T*, which can be determined by the equation: $\sigma = \sigma_{\infty} \exp(-E_a/kT)$, where σ_{∞} is the theoretical maximal hole conductivity, *k* is the Boltzmann constant, T is the temperature and E_a is the thermal activation energy.[51]

Table 1. **Power Factors ($\mu WK^{-2}m^{-1}$) with respect to dopant concentration (mol %).**

Polymer	5 mol %	10 mol %	25 mol %	35 mol %	50 mol %
PNTz4T_B(C_6F_5)$_3$	0.69	7.99	1.53	1	0.7
PNTz4T_B(C_6F_5)$_3$:diF-TES-ADT	3	26	11	5	1
PNTz4T_B(C_6F_5)$_3$:DTT-12	1.94	13.4	10	4	3
PBTTT_B(C_6F_5)$_3$	1.03	3.28	3.9	7.2	6.9
PBTTT_B(C_6F_5)$_3$:diF-TES-ADT	1.3	15.7	10.4	34.9	17.1
PTAA_B(C_6F_5)$_3$	0.11	0.47	0.25	0.13	0.04
PTAA_B(C_6F_5)$_3$:diF-TES-ADT	0.11	0.30	0.13	0.03	0.07

To increase the clarity of the conduction mechanisms, we performed temperature-dependent conductivity studies by both 4-point probe (**Figure S29-S32, SI**) and 2-terminal (with gate voltage V_G=0) (**Figure S33-S36, SI**) methods. For this measurement, we selected the film of the polymer that incorporates the maximum mol % of the dopant (either B(C_6F_5)$_3$ or the adducts) (50 mol %). We also carried out a comparison with the corresponding (polymer:conjugated molecule blend) of similar composition (50 mol % with respect to the polymer) for PNTz4T and PBTTT. All polymers exhibit a linear dependence of ln(conductivity) versus reciprocal temperature (**Figure S37, SI**). Values of the thermal activation energy of carrier hopping are collected in **Table S8, S9, S10, SI** for PNTz4T, PBTTT and PTAA for 4-point probe measurements, respectively. The results can be explained as follows: [a] Higher values of E_a for the adduct-doped samples indicate a contribution from transport barriers associated with higher voltage or more resistive domains across which carriers must traverse. [b] It is possible that the stability of either or both of the ions is also temperature-dependent. [c] Different adduct configurations with varied thermodynamic stabilities could form. [d] A weak temperature dependence of electrical conductivity (σ) as seen for polymers doped with B(C_6F_5)$_3$. This implies that the Fermi level is near the energy level where the charges are moving, and there are no

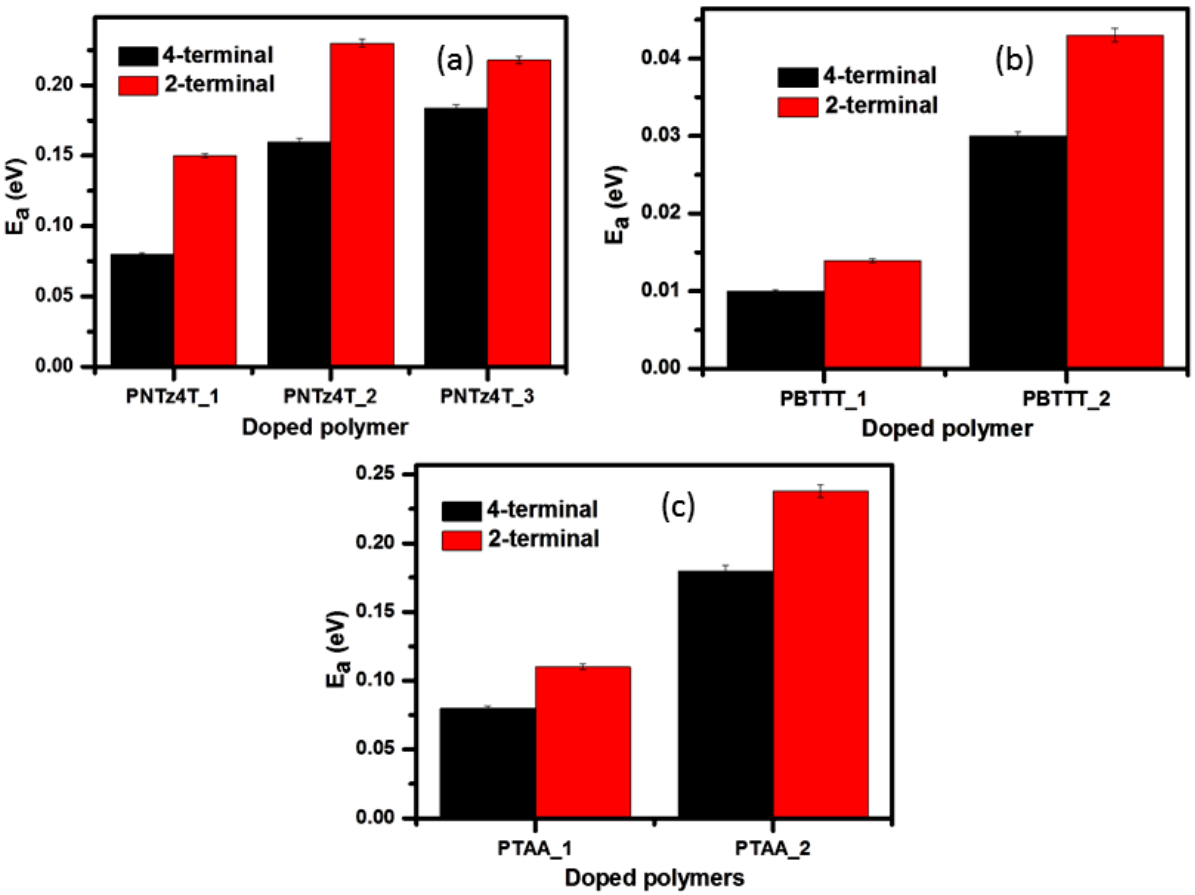

Figure 6. Comparison of activation energies obtained from temperature dependent conductivity measurement for (a), (b) PNTz4T (c), (d) PBTTT (e), (f) PTAA. PNTz4T_1 stands for PNTz4T doped with $B(C_6F_5)_3$ (50 mol %), PNTz4T_2 stands for PNTz4T doped with $B(C_6F_5)_3$: DTT-12 (50 mol %) and PNTz4T_3 stands for PNTz4T doped with $B(C_6F_5)_3$:DTT-12 (50 mol %). PBTTT_1 stands for PBTTT doped with $B(C_6F_5)_3$ (50 mol %) and PBTTT_2 stands for PBTTT doped with $B(C_6F_5)_3$: diF-TES-ADT (50 mol %). PTAA_1 stands for PTAA doped with $B(C_6F_5)_3$ (50 mol %) and PTAA_2 stands for PTAA doped with $B(C_6F_5)_3$: diF-TES-ADT (50 mol %).

strong barriers to charge hopping from molecule to molecule. When adducts are introduced to the polymeric systems, this creates a larger spread in site energies, E_{ij}, leading to greater width of the energy distribution. Therefore, larger thermal energies are needed to achieve a network with sites having similar energies.[48]

The E_a values extracted from 2-point probe measurements are listed in **Table S11, S12, S13** in the SI for PNTz4T, PBTTT and PTAA, respectively.[52,53,54] The trends in the E_a values are similar to those obtained by 4-point probe measurements (**Figure 6**) and the values are experimentally similar, suggesting that contact resistance has a negligible effect or no role to play in deciding the E_a values.

2.2.2. OFET studies

The transfer and output characteristics of the neat polymers (PNTz4T, PBTTT and PTAA) are

shown in **Figure S39-S41, SI** respectively, and the threshold voltages and hole mobilities are collected in **Table S14, SI**. For this study, we chose the least doped film (5 mol % dopant) to avoid charge carrier leakage through the gate electrode. The transfer characteristics of the field-effect transistors (OFETs) fabricated from 5% doped ($B(C_6F_5)_3$ and $B(C_6F_5)_3$:diF-TES-ADT/ $B(C_6F_5)_3$:DTT-12 as dopants) are shown in **Figure S42, SI** and the mobility and threshold voltages are extracted from plots of $I_{DS}^{1/2}$(A) versus V_G (V), as shown in **Figure S43, SI. T**he values are collected in **Table S15, SI**. For PNTz4T, PBTTT and PTAA, we observed that the borane dopant caused a more positive threshold voltage and higher mobility. The $B(C_6F_5)_3$:diF-TES-ADT/ $B(C_6F_5)_3$:DTT-12 dopants caused negligible change to the mobilities compared to the neat polymer and caused the threshold voltages to either become more negative or remain similar to the value of the neat polymer. The more negative V_{th} values are indicative of deeper electronic (trap states) in the band, as discussed in the previous section. Since more positional and energetic disorder has now been introduced in the polymeric system after the introduction of $B(C_6F_5)_3$:diF-TES-ADT/ $B(C_6F_5)_3$:DTT-12 dopants, it is also possible that, strong charge-phonon coupling occurs which leads to hole carrier self- trapping or a scattering of the hole carriers that reduces the mobility.[55,45,56] In OFETs, the charge transport is typically confined to the first few monolayers of the organic semiconductors adjacent to the gate dielectric,[57] so the transistor performance is greatly influenced by the interfacial dipoles which change the energy distribution of nearby hopping sites.[58]

2.2.3. Remote Gate platform for doping study

Jang *et al.* recently described an alternative method to characterize dopant effects and diffusion in polymers using a remote-gate (RG) field transistor setup which enables monitoring of the surface potential of the polymer film that is coupled to the oxide gate of a commercial silicon FET and is in series with a "remote" gate electrode and an acetonitrile (ACN) solution between the electrode and the film.[59] We employed this platform to estimate the charge carrier density as a result of doping of the polymers PNTz4T, PBTTT and PTAA with $B(C_6F_5)_3$, $B(C_6F_5)_3$:diF-TES-ADT and $B(C_6F_5)_3$:DTT-12 by solutes in ACN. The polymeric sensing layer was spin-coated onto a Si/SiO_2 (300 nm thermal oxide) substrate. If there is any change in the surface potential of the polymer film, the FET will report this change by means of the $V_{th,RG}$ shift. Depending on the direction and magnitude of this shift, we can gain information about the mechanism of interaction between the polymer layers and solutes in the ACN.

Figure S44-S47, SI displays the transfer curves of the RG FET coupled with each of our polymer sensing layers. Initially, we obtain the baseline $V_{th,RG}$ of our FET when the polymer film is equilibrated with neat ACN. After that, we add a drop (30 µl) of each concentration (in increasing order of concentration: 100 ng/ml, 1 µg/ml, 10 µg/ml, 100 µg/ml, 1 mg/ml) of a particular dopant and then re-measure the RG field effect transistor. For every dopant, we see a horizontal shift to the left which indicates an additional positive interfacial potential on the polymer film relative to that of the solution compared to that using neat ACN, a consequence of induced holes in the polymer layer and counterions

closer to the ACN. **Figure 7** (**Figure S48, SI** for the controls) represents the variation of the $V_{th,RG}$ with twenty consecutive scans, applied to determine stability or possible drift in response to the added dopant. Once the RG system is stabilized with ACN (10-20 scans), we obtain a modest drift. However, the drift magnitude is higher when the polymer is doped with $B(C_6F_5)_3$: diF-TES-ADT/ $B(C_6F_5)_3$: DTT-12 (for all mentioned dopant concentrations) than when it is doped with $B(C_6F_5)_3$. This may imply some form of a configurational rearrangement that occurs on a slower time scale for the adducts.

In order to extract hole concentration and mobility changes induced by dopants, we use two equations, as we have done in prior work:[77]

$$\sigma = \rho\, e\mu \qquad [1]$$

$$\rho_d = \rho_o \exp(-\Delta V_{th,RG}/kT) \qquad [2]$$

where σ is defined as the experimental four-point-probe conductivity, μ_h is the hole mobility, and ρ is the carrier concentration (ρ_o and ρ_d are the carrier concentrations without and with doping, respectively). $\Delta V_{th,RG}$ was extracted from the FET transfer curve shift. Changes in $\Delta V_{th,RG}$ values are shown in the form of a plot in **Figure S48, SI.** The value of $\Delta V_{th,RG}$ was extracted from the FET transfer curve shift. A reasonable estimate of the initial charge (hole) density, ρ_o, is required to apply equation [2]. To calculate the original charge densities (ρ_o), we used the charge densities, ρ_c , calculated by substituting the *σ values from the four-point conductivity measurements for every concentration of dopant added* (**Figure 4)** and the OFET mobility values for 5 wt% blended dopants (the highest doping that allowed OFET characterization) from **Table S15, SI** into Equation [1].

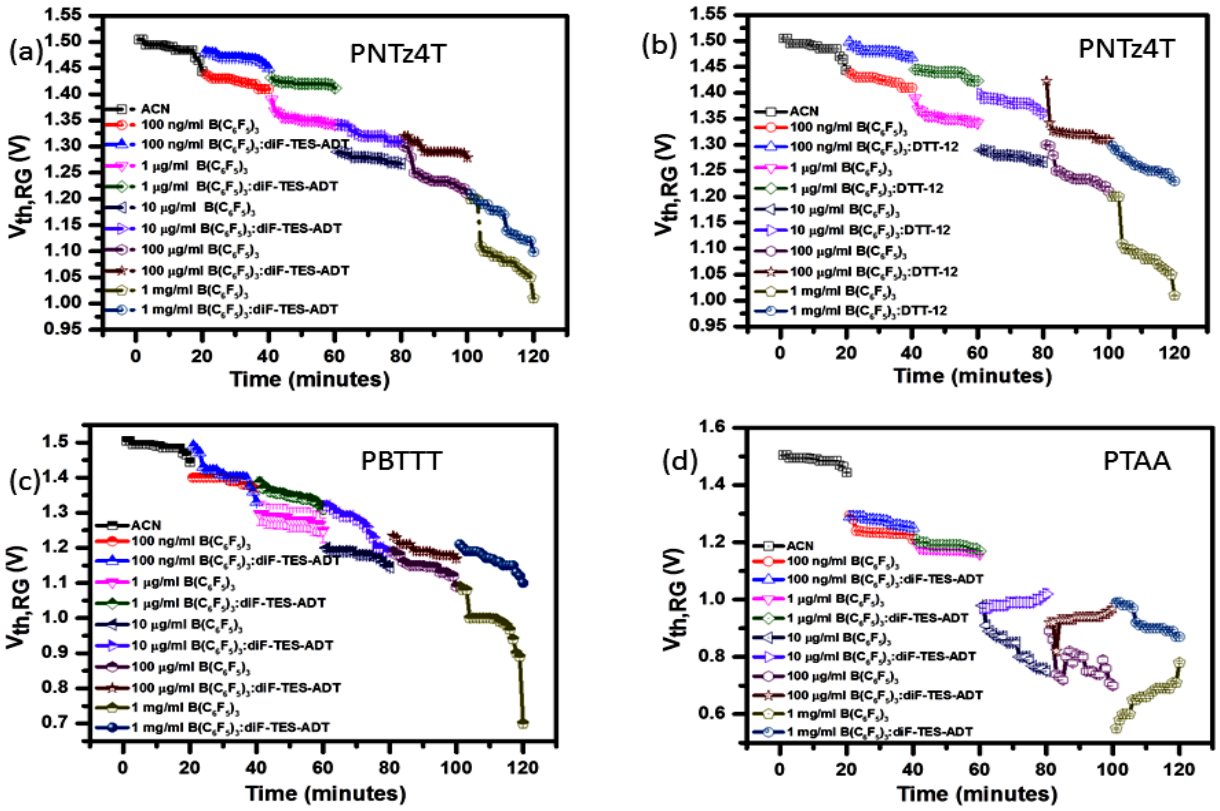

Figure 7. Changes to the $V_{th,RG}$ (V) during 20 consecutive scans for (a) PNTz4T (b) PBTTT (c) PTAA.

The resulting values of ρ_c extrapolated to zero dopant concentration give ρ_0. Rearranging equation [2] yields equation [3],

$$\ln\rho_d = \ln\rho_o - \Delta V_{th,RG}/kT \qquad [3]$$

Using the values of ρ_0 calculated for each polymer, a series of values of ρ_d were obtained for different concentrations of dopant species in the ACN solutions, as shown in **Tables S16, S17 and S18, SI**.

Tables S19, S20 and S21, SI (from **Figures S51**, **S52** and **S53**, **SI**) list ρ_d values calculated in three independent ways: from the capacitance times V_{th} determined near $V_G = 0$ in OFETs (Figures **S51**, **S52**, **S53, SI**) made from 5 mol % doped films, from four-point-probe conductivities measured on 5 mol % doped films divided by saturation OFET mobilities for those films, and from RG measurements on films with an arbitrary concentration of 100 ng/ml dopant in ACN. Similar values of ρ_d were obtained for each polymer-dopant combination using all three methods, *and more importantly, adducts gave charge densities that approached those from neat borane for all three polymers. This provides strong evidence that the adducts are capable of inducing mobile charges using multiple platforms. Also, when $B(C_6F_5)_3$ is added to the polymers first followed by diF-TES-ADT, we observed that the charge carrier density generated is in between those generated by direct doping with $B(C_6F_5)_3$ and $B(C_6F_5)_3$:diF-TES-ADT/ $B(C_6F_5)_3$:DTT-12 (**Table S16, S17, S18, SI**) and this has again been verified by multiple platforms (**Table S19, S20, S21**).*

In order to corroborate our electrical measurements, we carried out EPR spectroscopy of the doped solutions (50 mol % of dopants) of PBTTT, which exhibited the best performance in this study, in solution. The spectra are shown in **Figure S54, SI**. We observed that the radical density was the highest when PBTTT was doped with $B(C_6F_5)_3$ (50 mol %), compared to $B(C_6F_5)_3$:diF-TES-ADT (50 mol %). ESR spectroscopy confirms that, when $B(C_6F_5)_3$ is added to PBTTT first followed by diF-TES-ADT, the charge separation efficiency to form free carriers from the radicals is intermediate; that is, lower than when $B(C_6F_5)_3$ is employed as the dopant but greater than when adduct is employed as a dopant. Since the Wheland complexes themselves do not exhibit EPR signals, this confirms that the adducts/Wheland complexes are themselves dopants.

2.3. Polymer Film Physical Analysis

2.3.1. X-Ray Diffraction and Microscopy

For this study, we selected polymer films doped with 50 mol % of the dopant. X-ray diffraction analysis was carried out to evaluate the effect of the dopants on the microstructure and solid-state packing in the film (**Figure S55, SI)**. For PNTz4T, the 2θ values correspond to a sharp peak at 7.9° and a broad peak ~15° to 25°, which correspond to *d*-spacings of **10.9, 4.3-1.8 Å**. Once doped with $B(C_6F_5)_3$, all the peaks disappear, revealing significant incorporation/absorption of the dopant in the lamellae. *On doping with $B(C_6F_5)_3$:diF-TES-ADT, there is a complete disappearance of the peak at 7.9° and a very slight retention of the broad peak, which is seen to merge into one peak accompanied by a slight shift to a lower angle, implying an increase in the d-spacing between the corresponding crystallites.* This shows that both $B(C_6F_5)_3$ and $B(C_6F_5)_3$:diF-TES-ADT are encapsulated to different degrees in the polymer stacks and both cause significant disruption to the polymer morphology. PBTTT has an inherent crystallinity, with a *d*-spacing of **9.7 Å** corresponding to 8.85°. Once doped with $B(C_6F_5)_3$, the peak shifts to lower angle (6.7°) implying an increment in *d*-spacing ~**12.8 Å**. $B(C_6F_5)_3$: diF-TES-ADT also causes a similar shift; however, the peak intensity is higher. It is important to note that there is no peak at ~5° (**Figure 2**), which implies that there is no contribution from neat diF-TES-ADT. This constitutes additional evidence that it completely dopes in the complexed form. For PTAA, there is no inherent crystallinity, hence further changes in solid-state microstructure and packing could not be monitored by XRD.

We carried out microscopic characterization of neat polymer films and post-doping with $B(C_6F_5)_3$. We observed that, for all polymers, doping significantly alters the thin-film morphology (**Figure S56, SI**). For PNTz4T and PBTTT, the neat polymer films possess large and closely packed macrostructures/grains throughout the film. Once doped, the macrostructures are noticeably less dense and less prone to coalesce, which also explains the loss of lamellar packing due to dopant intercalation, as explained earlier. PTAA exhibits larger aggregates/grains compared to its neat film counterpart.

Since PBTTT exhibited the best performance in this series of polymers, we carried out SEM-EDS for PBTTT films for various dopants: ($B(C_6F_5)_3$; adduct $B(C_6F_5)_3$: diF-TES-ADT); and its control (**Figure S57, SI** and **Figure S58, SI**). Film elemental compositions are collected in **Table S22, S23, SI**. **Figure S57, SI (a)** shows the aggregates of similar shape as that of $B(C_6F_5)_3$as seen before, indicating an even distribution of $B(C_6F_5)_3$. As also corroborated by **XRD** studies, $B(C_6F_5)_3$ enters the crystalline regions of PBTTT and disrupts the crystallinity. **Table S23, SI** reveals that the PBTTT film doped with $B(C_6F_5)_3$: diF-TES-ADT (adduct) has S: F ratio~1.5-1.8 (~2) (vs. ~3, the stoichiometric ratio for PBTTT:($B(C_6F_5)_3$:diF-TES-ADT 50 mol %) for most of the spots (compared to the S:F ratios when PBTTT is doped with $B(C_6F_5)_3$ (**Table S22, SI**)). This supports a fairly even distribution of polymer (PBTTT): adducts throughout the PBTTT film matrix; thereby implying that adducts indeed form complexes with the polymer (seen also in the XRD diffractograms in **Figure S55 (b), SI** where the adduct does cause a crystallinity collapse of PBTTT). Results in **Figures S58, SI** indicate that by adding $B(C_6F_5)_3$ first, followed by diF-TES-ADT, the distribution of S and F with respect to each other is different from the morphology of the PBTTT film doped with $B(C_6F_5)_3$:diF-TES-ADT.

Figure S59, SI shows the PNTz4T thin film morphology with the addition of various dopants. **Table S24, SI** shows the elemental composition analysis of PNTz4T film doped with 50 mol % $B(C_6F_5)_3$: diF-TES-ADT adduct. Corresponding to **Figure S59 (a), SI (Table S24, SI)**; spots 1-3 show low F content. Spots 5-8 show a large percentage of F atoms, indicating that the region has a high concentration of $B(C_6F_5)_3$. Spots 1 and 11 hardly show F signals, indicating the presence of PNTz4T aggregates. The nature of the aggregates in this region can be assigned to PNTz4T based on the circular aggregates characteristic of the microscopy of the neat PNTz4T films in **Figure S56 (a), SI**. Spots 3-7 can be assigned as regions doped with $B(C_6F_5)_3$:diF-TES-ADT. Spots 2, 8-10, 12, 13 indicate large amounts of the diF-TES-ADT conjugated molecule. Thus, when PNTz4T film is doped with adduct $B(C_6F_5)_3$:diF-TES-ADT, a large degree of phase segregation is observed. **Figure S56 (b)** and **Figure S59 (b), SI** (in greater detail) depicts the morphological features and elemental composition of PNTz4T film doped with adduct $B(C_6F_5)_3$: DTT-12. The film shows crystallites typical of DTT-12 (observed in **Figure S17 (d), SI**). The XRD-diffractogram of the film (**Figure S60, SI)** reveals the presence of free DTT-12, which may point to the tendency of DTT-12 to show a strong drive to crystallize back or reversible complexation at the adduct-formation stage. Because of a low degree of complexation, $B(C_6F_5)_3$:DTT-12 had exhibited a lesser degree of dopant activity in our electrical characterization studies shown earlier. Overall for PNTz4T, the morphology of the film is seen to be largely different when $B(C_6F_5)_3$ is used as a dopant versus $B(C_6F_5)_3$:diF-TES-ADT or $B(C_6F_5)_3$:DTT-12 (adducts).

PTAA exhibited oval-shaped structures (**Figure S61, SI**) shown at various magnifications. This type of morphology was not observed in the microscopic images of neat PTAA films or $B(C_6F_5)_3$-doped PTAA film (**Figure S56, SI**). **Table S25, SI** reveals the elemental composition of spots 6 and 7. The presence of both S and F signals (given that there is no contribution of the PTAA to the S signal) indicate

the polymer-dopant complexation or incorporation of $B(C_6F_5)_3$: diF-TES-ADT into the polymer matrix.

Our microstructural packing and morphological studies support the trends in conductivity and Seebeck coefficients discussed earlier. A greater disruption/collapse of crystallinity is caused by $B(C_6F_5)_3$ than adducts $B(C_6F_5)_3$: diF-TES-ADT/$B(C_6F_5)_3$:DTT-12. Moreover, there appears to be a more uniform distribution of $B(C_6F_5)_3$ throughout the polymer films than adducts $B(C_6F_5)_3$: diF-TES-ADT/$B(C_6F_5)_3$:DTT-12, based on the S:F ratios obtained from SEM-EDS measurements, regardless of the fact that adducts do form complexes with the polymers. As also shown earlier in **Figure 3**, adducts themselves may aggregate into domains. Evidence points to more localized aggregation/phase segregation and chances of formation of charged grain boundaries in $B(C_6F_5)_3$: diF-TES-ADT/ $B(C_6F_5)_3$: DTT-12 doped polymer films. This leads to energy offsets at charged grain boundaries causing interfacial regions to be more resistive than bulk and also contribute to higher Seebeck coefficients. Also, there can be band offsets at grain boundaries. Structural differences at grain boundaries created due to factors such as lattice mismatch due to introduction of the conjugated molecule (while doping with adducts) also cause adduct-doped polymers to be more resistive than borane-doped polymer films.[60,61] Therefore, to avoid the lattice mismatch, the ideal choice of small molecules to study the formation/effects of adducts is to generate the adducts using polymer segments themselves, but this is difficult to achieve and will be a subject of further study.

2.3.2. Polymer film steady-state spectroscopy

Changes to the UV-visible spectra of PNTz4T, PBTTT and PTAA caused by doping are shown in **Figure S62, SI**. Polymer films doped with 50 mol % of dopant were selected as subjects for this study. The peak corresponding to polaron formation and evolution is shown in the form of an arrow. Part **(a)** of that figure shows that PNTz4T has a strong absorption peak between 800-500 nm. On doping with $B(C_6F_5)_3$, this peak splits into two vibronic features. A similar splitting is observed on doping with $B(C_6F_5)_3$:diF-TES-ADT, accompanied by an enhancement in the absorption features between 650-550 nm, which includes a contribution from the diF-TES-ADT component. The absorption spectra of the PNTz4T_diF-TES-ADT neat blend (in the same window) confirms this contribution of diF-TES-ADT to the absorption peak~650-550 nm. The absorption feature ~800 nm-650 nm can be assigned to the polaronic evolution, its intensity being relatively higher for $B(C_6F_5)_3$ (50 mol %) incorporation in PNTz4T matrix, followed by $B(C_6F_5)_3$:diF-TES-ADT (50 mol %) and $B(C_6F_5)_3$:DTT-12 (50 mol %). This absorption feature is absent in neat PNTz4T and PNTz4T conjugated molecule (diF-TEs-ADT/DTT-12) addition.

Figure S62, SI (b) shows the changes in the UV-visible spectra of PBTTT on doping. A shoulder starts to evolve on dopant addition. On doping with $B(C_6F_5)_3$ and $B(C_6F_5)_3$:diF-TES-ADT,

new absorption features arise ~700-600 nm, which is not seen in case of PBTTT_diF-TES-ADT (50 mol %) neat blends. **Figure S62, SI (c)** reveals changes in the UV-visible spectra of PTAA on doping. The peak ~650-500 nm shows a relative increase in intensity.

In summary, the UV-visible spectra of the doped polymers reveal the evolution of similar vibronic features at higher wavelengths, on doping with $B(C_6F_5)_3$ and $B(C_6F_5)_3$:diF-TES-ADT/ $B(C_6F_5)_3$:DTT-12. The relative intensities of the evolving vibrational features (polaron peak) are higher on employing $B(C_6F_5)_3$ as a dopant compared to the adducts.

Based on our experimental results, we propose a mechanism illustrated in **Figure 8**. For illustration purposes, we have shown the mechanism only with diF-TES-ADT. DTT-12 is also expected to follow a similar mechanism, except the DTT-12 would be the coordinating ligand to BCF instead of diF-TES-ADT.

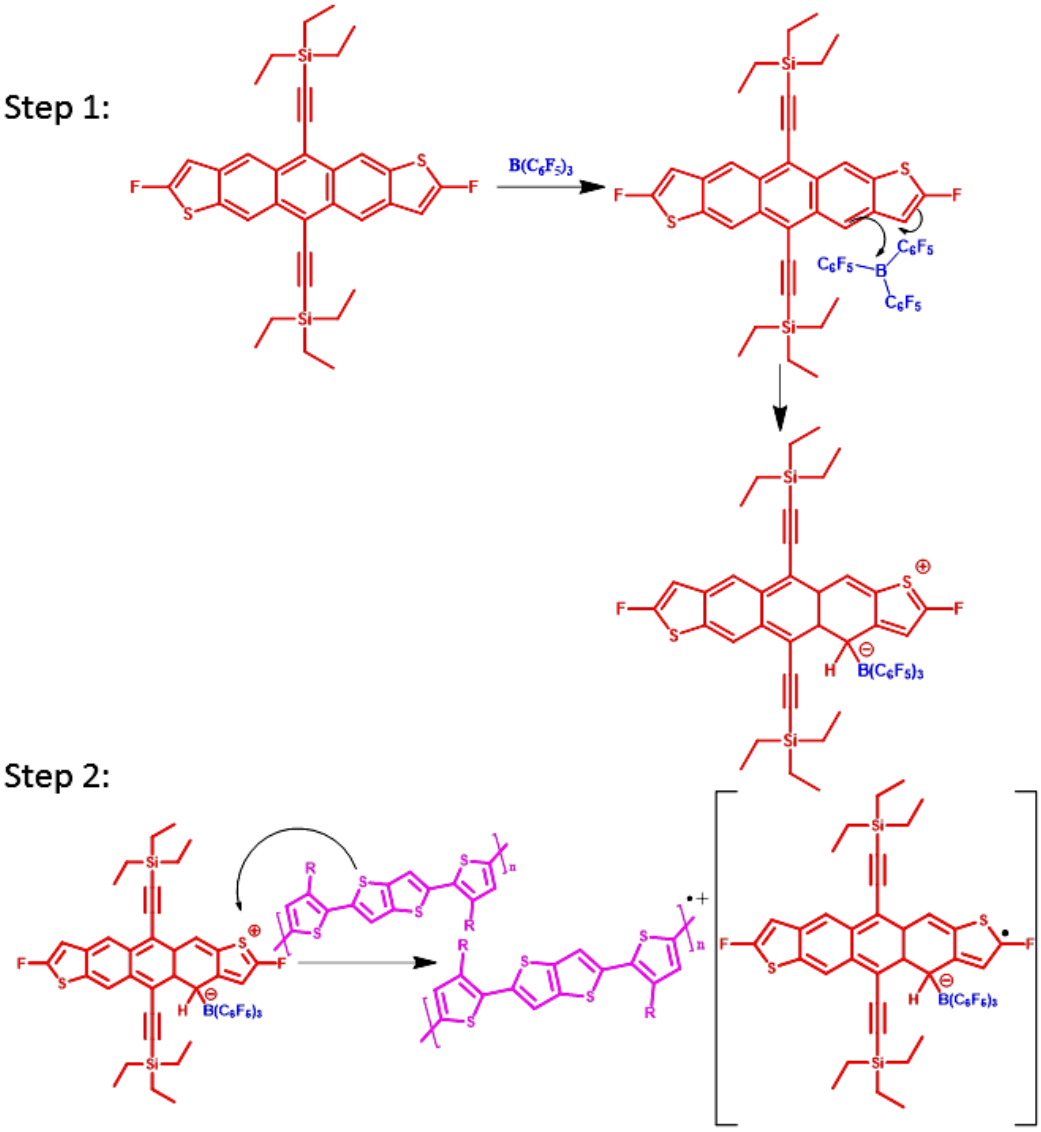

Figure 8. Doping mechanism proposed in this work, based on our results.

Additional insights into the stability and integrity of the Wheland complexes/adducts: We performed ^{11}B NMR to monitor the chemical environment of the B atom in $B(C_6F_5)_3$ under different doping conditions, namely (a) neat $B(C_6F_5)_3$ in $CDCl_3$ (b) $B(C_6F_5)_3$:diF-TES-ADT (c) on doping PBTTT with 50 mol % $B(C_6F_5)_3$ (d) on doping PBTTT with 50 mol % of $B(C_6F_5)_3$:diF-TES-ADT and (e) on doping PBTTT with 50 mol % of $B(C_6F_5)_3$ addition followed by diF-TES-ADT addition (50 mol %). The chemical shifts of the B atom, under the above-mentioned conditions are ^{11}B NMR ($CDCl_3$, 300 MHz) (a) δ53.20, 42.29 ppm (b) δ 41.02 ppm (c) δ 40.28 ppm (d) δ 41.61 ppm (e) δ 41.36 ppm and (f) δ 41.26 ppm (**Figure S63, SI**). Note that the broad peak is a contribution from the probe that is made of borosilicate glass. The previously reported ranges of chemical shifts are: δ 50-70 ppm for Ar_3B (Ar=aryl), 40-50 ppm for R_2BOH, $RB(SR')_2$, 20-30 ppm for R_2NBF_2.[62] Based on this analogy and the possible binding sites of the B atom in our systems (as seen from ^1H NMR spectra and computations), we observed the following: (a) it is possible that the $B(C_6F_5)_3$ is partially hydrolysed in $CDCl_3$ to form species of the type R_2BOH (δ 42.29 ppm) (**Figure S63, (a), SI**) while the free, uncomplexed B atom

exhibits δ53.20 ppm. (b) on complexation with diF-TES-ADT, the peak corresponding to the population of uncomplexed B atoms in the sample disappeared and entered into complexation with the C=C bonds in the benzene rings and S atoms (**Figure S5, SI**) to exhibit a more shielded chemical environment corresponding to δ41.02 ppm. (c) on addition of 50 mol % borane (BCF) to PBTTT polymer, a further shielding effect was observed to cause the chemical shift of the B atom in $B(C_6F_5)_3$ to δ40.28 ppm from δ 42.29 ppm. (d) on addition of the Wheland complex $B(C_6F_5)_3$:diF-TES-ADT (50 mol %) to PBTTT, the chemical environment of the B atom changes such that the chemical shift is now δ41.61 ppm, which is different from the case (c) of the neat BCF dopant (e) on addition of 50 mol % $B(C_6F_5)_3$ followed by the addition of diF-TES-ADT to PBTTT polymer; the chemical shift is now δ41.36 ppm, which is in closer resemblance with the chemical shift of the B atom δ41.02 which was assigned to the B atom in the Wheland complex, rather than uncomplexed B atom (which would have been created in solution had the adduct disintegrated as diF-TES-ADT and $B(C_6F_5)_3$. The polymer (PBTTT) was precipitated from the adduct-doped solution by adding anti-solvent methanol, so that the polymer precipitated out of the solution as a powder. The supernatant liquid was filtered, collected and dried under high vacuum and then dissolved in $CDCl_3$ to acquire ^{11}B NMR. This indicates that the adduct or Wheland complex may have been intact throughout the doping process instead of splitting up, to a large degree and (f) the ^{11}B NMR of the precipitated solid (caption of **Figure S63, SI**) showed that the chemical shift of the B atom is δ41.26 ppm which is in closer agreement with that of the B atom in the Wheland complex $B(C_6F_5)_3$:diF-TES-ADT. This implies that the addition of methanol does not perturb the $B(C_6F_5)_3$/diF-TES-ADT interactions, which also validates the integrity of the adduct during the doping process. This can be corroborated by the bond energy (BE) or bond enthalpy values; which are slightly less negative than those of $B(C_6F_5)_3$: diF-TES-ADT (**Figure S5, Table S3, SI**).

We also performed ^{11}B NMR to study the chemical environment of the B atom in $B(C_6F_5)_3$ under different doping conditions, namely (a) neat $B(C_6F_5)_3$ in $CDCl_3$ (b) $B(C_6F_5)_3$:DTT-12 (c) on doping PNTz4T with 50 mol % $B(C_6F_5)_3$ (d) on doping PNTz4T with 50 mol % of $B(C_6F_5)_3$:DTT-12 and (e) on doping PNTz4T with 50 mol % of $B(C_6F_5)_3$ addition followed by DTT-12 addition (50 mol %). The chemical shifts of the B atom, under the above-mentioned conditions are ^{11}B NMR ($CDCl_3$, 300 MHz) (a) δ53.20, 42.29 ppm (b) δ 41.29 ppm (c) δ 40.77, 24.51 ppm (d) δ 40.77, 24.51 ppm (e) δ 40.79, 25.08 ppm and (f) δ 40.78, 24.28 ppm (**Figure S64, SI**). Based on the possible binding sites of the B atom in PNTz4T (as seen from ^1H NMR spectra and computations), we observed that on complexation with DTT-12, the B atom is now in a more shielded environment and there is no trace of uncomplexed B atoms (the absence of the δ 53.20 ppm). On addition of 50 mol % borane (BCF) to PNTz4T, the B atom experienced a further shielding effect (δ 40.77 ppm). On addition of the Wheland complex $B(C_6F_5)_3$:DTT-12 (50 mol %) to PNTz4T, the chemical environment of the B atom changes such that the chemical shift is now δ40.79 ppm, which is similar to the chemical environment of the B atom when PNTz4T is doped with $B(C_6F_5)_3$ (δ40.77 ppm). On addition of 50 mol % $B(C_6F_5)_3$ followed

by the addition of DTT-12 to PNTz4T polymer; the chemical shift is now δ40.78 ppm, which is in closer resemblance with the chemical shift of the B atom both when it is introduced into PNTz4T as $B(C_6F_5)_3$ as well as $B(C_6F_5)_3$:DTT-12. Therefore, in this case it is possible that the most of the molecules of the adduct remain intact when it is employed as a dopant; because the chemical shift of the B atom in this case is similar to the chemical shift of the B atom when it exists as $B(C_6F_5)_3$:DTT-12 (**Figure S64, (b)**). However, we do not rule out the possibility that the some of the molecules of $B(C_6F_5)_3$ that is added first partially complexes with the polymer, while the remainder free borane forms Wheland complexes with diF-TES-ADT/DTT-12 and then participates in the doping process. It is difficult to quantify the concentrations due to difficulties associated with integration of broad ^{11}B NMR peaks and very close energies of interaction of $B(C_6F_5)_3$ with conjugated small molecules (**Figure S4, S5, Table S2, S3, SI**) as well as polymers (**Figure S65, S66, S67, SI**).

3. Computational Studies using Density Functional Theory:

A computational study using an *ab initio* approach was conducted to determine the likelihood of formation of the aforementioned complexes. We used the density functional theory software package, ORCA, to simulate the electronic structures and calculate the binding energies and electron affinities of the proposed adducts.[63,64] These calculations were performed in an "implicit" acetonitrile solvent, which essentially immerses the adducts in a medium that supplies a mean dielectric constant to the simulation environment. It was found that both the $B(C_6F_5)_3$: diF-TES-ADT and $B(C_6F_5)_3$:DTT-12 adducts had favorable binding enthalpies. Across all simulations, the details of which are provided in the **SI**, the former exhibited a mean binding enthalpy of -0.65 eV, and the latter exhibited a mean binding enthalpy of -0.58 eV. These negative values indicate that the adducts have lower energies than their individual components and are therefore more enthalpically stable. These values support the hypothesis that Wheland or Lewis base-Lewis acid complexes can indeed form.

Additionally, it was found that the electron affinity of each adduct approached that of lone $B(C_6F_5)_3$, rather than that of the conjugated molecule, as shown in **Figure S68, S69, SI**. That is, when forming a complex with $B(C_6F_5)_3$, the overall system exhibits an electron affinity (3.0-3.3 eV) that almost exactly matches that of $B(C_6F_5)_3$ by itself. This provides a reason why a Wheland or Lewis base complex can act as a comparably electron-attracting dopant compared to $B(C_6F_5)_3$.

We conducted a complementary study to assess the binding energies and ionization potentials of a hypothetical $B(C_6F_5)_3$:polymer segment structure for the polymers PNTz4T, PBTTT, and PTAA (**Figure S65, S66, S67, SI**). Using an identical technique as before, density functional theory was again used for this investigation. It was found that, for all three polymers listed, the average binding enthalpies of $B(C_6F_5)_3$ were very similar and favorable: -0.55 eV, -0.59 eV, and -0.63 eV, respectively, again indicating the relative stability of the adduct. Moreover, the ionization potentials of these adducts closely mirrored those of their constituent *polymers*, for which the values were 4.7-5.0 eV. These results

are compiled in **Figure S70, SI**. So far, we have found an enthalpic disfavoring of charge transfer from a neutral polymer to a conjugated molecule adduct of 1.5-1.8 eV, calculated as the difference between ionization potentials of the polymers (solid lines in **Figure S70, SI)** and electron affinities of conjugated molecule adducts **(dots in Figure S68, S69, SI).**

However, we also assessed the effect of Coulombic attraction between the polymer and the counterion formed by doping. Using a conjugated molecule adduct system according to the mechanism illustrated in **Figure 8**, we conducted simulations in which the entire adduct system was replaced by a singular "negative charge;" in this case, a chloride anion, which was then placed near the radical cation formed by doping of the polymer segments. It was found through these simulations that the doped polymer system exhibited an ionization potential more than 1 eV *lower* than its undoped counterpart, as compiled in **Figure S70, SI**. This compensates for more than half of the enthalpic disfavoring of the charge transfer. The remaining 0.5 eV or so of enthalpic opposition to doping could be accommodated by entropic contributions. Studies on polymer solar cells suggest that hole delocalization entropy contributes about 0.1-0.3 eV to the driving force for charge separation at room temperature. Increased dimensionality, meaning the expansion of charge location from a single atom on a molecule to the many atomic sites available in a volume of polymer matrix and the number of configurations available to large numbers of induced charge carriers, also increases this entropic driving force.[65,66,67,68] Thus, the addition of Coulombic and entropic effects to the calculated single molecule electron transfer energies brings the doping process close to the point of free energy neutrality, meaning that at equilibrium, some amount of adduct-based doping is possible.

4. Conclusions

The important observations that we obtained that support the role of our conjugated molecule adducts as direct dopants are as follows:

[A] The $B(C_6F_5)_3$:diF-TES-ADT adduct causes an increase in the *d*-spacing similar to $B(C_6F_5)_3$, which is indicative of adducts being capable of disruption of crystallinity during doping. The Wheland complexes $B(C_6F_5)_3$:diF-TES-ADT and $B(C_6F_5)_3$:DTT-12 did not exhibit signals in EPR and are confirmed to be spin-paired species. An upfield shift in the ^{11}B NMR confiirmed a coordinate bond formation.

[B] Use of $B(C_6F_5)_3$ leads to higher conductivities and mobilities than either ($B(C_6F_5)_3$:diF-TES-ADT) or ($B(C_6F_5)_3$:DTT-12). Thus, even though the adducts are less efficient dopants, their behavior is distinct from that of $B(C_6F_5)_3$ alone. Control experiments indicate that the adducts dope the polymers as one single, stable entity, as zwitterions, and do not split up to yield $B(C_6F_5)_3$ as the dopant. Control experiments also indicate a strong chance of adduct formation involving the $B(C_6F_5)_3$ and the added conjugated small molecule, such that it participates as a dopant along with BCF. The charge carrier

densitities generated in the controls is intermediate between those generated by direct doping with BCF and the adducts.

[C] The conductivity and Seebeck coefficients were clearly coupled, as expected. The higher Seebeck coefficients of the polymer films doped with the adducts eventually dominates and leads to higher power factors, as shown for both PBTTT and PNTz4T. Additonally, it is important to note that $B(C_6F_5)_3$:diF-TES-ADT leads to higher power factors than $B(C_6F_5)_3$:DTT-12. It was shown before by morphology studies that DTT-12 has a strong tendency to recrystallize. In the remote gate experiments, $B(C_6F_5)_3$:diF-TES-ADT produces higher charge densities than $B(C_6F_5)_3$:DTT-12. Thus, the structure of the adduct plays a very important role in the doping process, evidence for the adduct staying intact in each mixture.

[D] Charge densities were induced by adducts that were within an order of magnitude, and sometimes in closer agreement, with values obtained using the boranes alone, from three independent measurement methods.

[E] ^{11}B NMR reveals that adducts can in fact form in the control case, because of the resemblance of the chemical environment of the B atom when BCF is added to the polymer first, followed by oligomer addition; to the chemical environment of the B atom in the Wheland complex/adduct dopant. On selective precipitation of the polymer PBTTT from the doped solution, the ^{11} B NMR specra of the solid recovered (post processing) confirmed a high probability of the integrity of the adduct. EPR spectra corroborates that there is partly contribution of adducts as well as neat BCF in the doping process.

[F] Complementary DFT studies provided justification for the formation of $B(C_6F_5)_3$:conjugated molecule adducts. The favorability of these adducts to form was demonstrated from a binding enthalpy standpoint. Furthermore, justification is provided for the possibility of adduct doping through calculations of ionization potential and electron affinity, including Coulombic and entropic effects.

A recent paper about the capability of B-OH species to serve as proton dopants invoked formation of bridging protonated oxygens between boranes as energetically favorable dopants.[32] The analogous species in this study would be an “conjugated molecule” with two boranes attached, which would be more electron deficient than the adducts of this study and provide increased driving force for covalent adduct doping, which justifies our proposed mechanism (**Figure S57, SI**).[32] Our studies clearly show that adducts can act as dopants. Since different electrical and morphological properties were obtained and were strongly a function of the nature of the conjugated molecule involved in formation of the complexes, we propose they they should be considered as alternatives along with BOH species. Our experimental and theoretical studies are, thus, in excellent agreement with the mechanism proposed in **Figure S57, SI**.

ACKNOWLEDGMENTS

This work was primarily supported by the National Science Foundation, Division of Chemistry, grant numbers 1708245 and 2107360. The x-ray diffraction and SEM-EDS studies were supported by U.S. Department of Energy, Office of Science, Basic Energy Sciences, Materials Chemistry Program, under Award number DE-FG02-07ER46465. Computational work was carried out at the Advanced Research Computing at Hopkins (ARCH) core facility (rockfish.jhu.edu), which is supported by the National Science Foundation (NSF) grant number OAC 1920103. CG and PC gratefully acknowledge support of computational work from the Whiting School of Engineering at Johns Hopkins University. We thank Nan (Louise) Chen for helpful assistance and guidance about the Seebeck coefficient measurements, Jonathan Catazaro JHU NMR Facility Director, for assistance with boron NMR, and Dr. Jinfeng Han for assistance with EPR.

Supporting Information

The Supporting Information is available free of charge at https://pubs.acs.org. Experimental details, ^{1}H NMR spectra of Wheland complexes and ^{11}B NMR of doped polymers, conductivity and Seebeck study plots, microscopy and SEM-EDS analyses, optimized Wheland complex geometries and computational details.

REFERENCES

(1) Goel, M.; Thelakkat, M. Polymer Thermoelectrics: Opportunities and Challenges. *Macromolecules* **2020**, *53*, 3632–3642. https://doi.org/10.1021/acs.macromol.9b02453.

(2) Zhao, W.; Ding, J.; Zou, Y.; Di, C.; Zhu, D. Chemical Doping of Organic Semiconductors for Thermoelectric Applications. *Chem. Soc. Rev.* **2020**, *49*, 7210–7228. https://doi.org/10.1039/D0CS00204F.

(3) Yoon, S. E.; Kang, Y.; Jeon, G. G.; Jeon, D.; Lee, S. Y.; Ko, S.-J.; Kim, T.; Seo, H.; Kim, B.-G.; Kim, J. H. Exploring Wholly Doped Conjugated Polymer Films Based on Hybrid Doping: Strategic Approach for Optimizing Electrical Conductivity and Related Thermoelectric Properties. *Adv. Funct. Mater.* **2020**, *30*, 2004598. https://doi.org/https://doi.org/10.1002/adfm.202004598.

(4) Liang, Z.; Zhang, Y.; Souri, M.; Luo, X.; Boehm, A. M.; Li, R.; Zhang, Y.; Wang, T.; Kim, D.-Y.; Mei, J.; Marder, S. R.; Graham, K. R. Influence of Dopant Size and Electron Affinity on the Electrical Conductivity and Thermoelectric Properties of a Series of Conjugated Polymers. *J. Mater. Chem. A* **2018**, *6*, 16495–16505. https://doi.org/10.1039/C8TA05922E.

(5) Di Nuzzo, D.; Fontanesi, C.; Jones, R.; Allard, S.; Dumsch, I.; Scherf, U.; von Hauff, E.; Schumacher, S.; Da Como, E. How Intermolecular Geometrical Disorder Affects the Molecular Doping of Donor–Acceptor Copolymers. *Nat. Commun.* **2015**, *6*, 6460. https://doi.org/10.1038/ncomms7460.

(6) Lindorf, M.; Mazzio, K. A.; Pflaum, J.; Nielsch, K.; Brütting, W.; Albrecht, M. Organic-Based Thermoelectrics. *J. Mater. Chem. A* **2020**, *8*, 7495–7507. https://doi.org/10.1039/C9TA11717B.

(7) Ray, S.; Panidi, J.; Mukhopadhyay, T.; Salzner, U.; Anthopoulos, T. D.; Patil, S. Electrochemical Stability and Ambipolar Charge Transport in Diketopyrrolopyrrole-Based Organic Materials. *ACS Appl. Electron. Mater.* **2019**, *1*, 2037–2046. https://doi.org/10.1021/acsaelm.9b00394.

(8) de Boor, J.; Müller, E. Data Analysis for Seebeck Coefficient Measurements. *Rev. Sci. Instrum.* **2013**, *84*, 65102. https://doi.org/10.1063/1.4807697.

(9) Jung, I. H.; Hong, C. T.; Lee, U.-H.; Kang, Y. H.; Jang, K.-S.; Cho, S. Y. High Thermoelectric Power Factor of a Diketopyrrolopyrrole-Based Low Bandgap Polymer via Finely Tuned Doping Engineering. *Sci. Rep.* **2017**, *7*, 44704. https://doi.org/10.1038/srep44704.

(10) Culebras, M.; Gómez, C. M.; Cantarero, A. Review on Polymers for Thermoelectric Applications. *Materials* . 2014. https://doi.org/10.3390/ma7096701.

(11) Bridges, C. R.; Baumgartner, T. Lewis Acids and Bases as Molecular Dopants for Organic Semiconductors. *J. Phys. Org. Chem.* **2020**, *33*, 4077. https://doi.org/https://doi.org/10.1002/poc.4077.

(12) Huang, F.; MacDiarmid, A. G.; Hsieh, B. R. An Iodine-Doped Polymer Light-Emitting Diode. *Appl. Phys. Lett.* **1997**, *71*, 2415–2417. https://doi.org/10.1063/1.120078.

(13) Chen, Y.; Shih, I.; Xiao, S. Effects of $FeCl_3$ Doping on Polymer-Based Thin Film Transistors. *J. Appl. Phys.* **2004**, *96*, 454–458. https://doi.org/10.1063/1.1760838.

(14) Untilova, V.; Hynynen, J.; Hofmann, A. I.; Scheunemann, D.; Zhang, Y.; Barlow, S.; Kemerink, M.; Marder, S. R.; Biniek, L.; Müller, C.; Brinkmann, M. High Thermoelectric Power Factor of Poly(3-Hexylthiophene) through In-Plane Alignment and Doping with a Molybdenum Dithiolene Complex. *Macromolecules* **2020**, *53*, 6314–6321. https://doi.org/10.1021/acs.macromol.0c01223.

(15) Finn, P. A.; Jacobs, I. E.; Armitage, J.; Wu, R.; Paulsen, B. D.; Freeley, M.; Palma, M.; Rivnay, J.; Sirringhaus, H.; Nielsen, C. B. Effect of Polar Side Chains on Neutral and P-Doped Polythiophene. *J. Mater. Chem. C* **2020**, *8*, 16216–16223. https://doi.org/10.1039/D0TC04290K.

(16) Vijayakumar, V.; Durand, P.; Zeng, H.; Untilova, V.; Herrmann, L.; Algayer, P.; Leclerc, N.; Brinkmann, M. Influence of Dopant Size and Doping Method on the Structure and Thermoelectric Properties of PBTTT Films Doped with F_6TCNNQ and F_4TCNQ. *J. Mater. Chem. C* **2020**, *8*, 16470–16482. https://doi.org/10.1039/D0TC02828B.

(17) Karpov, Y.; Kiriy, N.; Al-Hussein, M.; Hambsch, M.; Beryozkina, T.; Bakulev, V.; Mannsfeld, S. C. B.; Voit, B.; Kiriy, A. Hexacyano-[3]-Radialene Anion-Radical Salts: A Promising Family of Highly Soluble p-Dopants. *Chem. Commun.* **2018**, *54*, 307–310. https://doi.org/10.1039/C7CC08671G.

(18) Lu, Y.; Yu, Z.-D.; Liu, Y.; Ding, Y.-F.; Yang, C.-Y.; Yao, Z.-F.; Wang, Z.-Y.; You, H.-Y.; Cheng, X.-F.; Tang, B.; Wang, J.-Y.; Pei, J. The Critical Role of Dopant Cations in Electrical Conductivity and Thermoelectric Performance of N-Doped Polymers. *J. Am. Chem. Soc.* **2020**, *142*, 15340–15348. https://doi.org/10.1021/jacs.0c05699.

(19) Kohno, S.; Yamashita, Y.; Kasuya, N.; Mikie, T.; Osaka, I.; Takimiya, K.; Takeya, J.; Watanabe, S. Controlled Steric Selectivity in Molecular Doping towards Closest-Packed Supramolecular Conductors. *Commun. Mater.* **2020**, *1*, 79. https://doi.org/10.1038/s43246-020-00081-3.

(20) Li, H.; DeCoster, M. E.; Ming, C.; Wang, M.; Chen, Y.; Hopkins, P. E.; Chen, L.; Katz, H. E. Enhanced Molecular Doping for High Conductivity in Polymers with Volume Freed for Dopants. *Macromolecules* **2019**, *52*, 9804–9812. https://doi.org/10.1021/acs.macromol.9b02048.

(21) Scholes, D. T.; Yee, P. Y.; McKeown, G. R.; Li, S.; Kang, H.; Lindemuth, J. R.; Xia, X.; King, S. C.; Seferos, D. S.; Tolbert, S. H.; Schwartz, B.J. Designing Conjugated Polymers for Molecular Doping: The Roles of Crystallinity, Swelling, and Conductivity in Sequentially-Doped Selenophene-Based Copolymers. *Chem. Mater.* **2019**, *31*, 73–82. https://doi.org/10.1021/acs.chemmater.8b02648.

(22) Wu, S.; Xing, W.; Zhu, M.; Zou, Y.; Sun, Y.; Xu, W.; Zhu, D. Doped Thieno[3,4-b]Thiophene-Based Copolymers for p-Type Organic Thermoelectric Materials. *J. Mater. Chem. C* **2021**, *9*, 4158–4163. https://doi.org/10.1039/D1TC00211B.

(23) Scholes, D. T.; Hawks, S. A.; Yee, P. Y.; Wu, H.; Lindemuth, J. R.; Tolbert, S. H.; Schwartz, B. J. Overcoming Film Quality Issues for Conjugated Polymers Doped with F4TCNQ by Solution Sequential Processing: Hall Effect, Structural, and Optical Measurements. *J. Phys. Chem. Lett.* **2015**, *6*, 4786–4793. https://doi.org/10.1021/acs.jpclett.5b02332.

(24) Zhao, X.; Madan, D.; Cheng, Y.; Zhou, J.; Li, H.; Thon, S. M.; Bragg, A. E.; DeCoster, M. E.; Hopkins, P. E.; Katz, H. E. High Conductivity and Electron-Transfer Validation in an n-Type Fluoride-Anion-Doped Polymer for Thermoelectrics in Air. *Adv. Mater.* **2017**, *29*, 1606928. https://doi.org/https://doi.org/10.1002/adma.201606928.

(25) Suh, E. H.; Oh, J. G.; Jung, J.; Noh, S. H.; Lee, T. S.; Jang, J. Brønsted Acid Doping of P3HT with Largely Soluble Tris(Pentafluorophenyl)Borane for Highly Conductive and Stable Organic Thermoelectrics Via One-Step Solution Mixing. *Adv. Energy Mater.* **2020**, *10*, 2002521. https://doi.org/https://doi.org/10.1002/aenm.202002521.

(26) Yee, P. Y.; Scholes, D. T.; Schwartz, B. J.; Tolbert, S. H. Dopant-Induced Ordering of Amorphous Regions in Regiorandom P3HT. *J. Phys. Chem. Lett.* **2019**, *10*, 4929–4934. https://doi.org/10.1021/acs.jpclett.9b02070.

(27) Han, C. C.; Elsenbaumer, R. L. Protonic Acids: Generally Applicable Dopants for Conducting Polymers. *Synth. Met.* **1989**, *30*, 123–131. https://doi.org/https://doi.org/10.1016/0379-6779(89)90648-6.

(28) Yan, H.; Ma, W. Making Weak Dopants Strong. *Nat. Mater.* **2019**, *18*, 1269–1270. https://doi.org/10.1038/s41563-019-0493-2.

(29) Mayer, R. J.; Hampel, N.; Ofial, A. R. Lewis Acidic Boranes, Lewis Bases, and Equilibrium Constants: A Reliable Scaffold for a Quantitative Lewis Acidity/Basicity Scale. *Chem. – A Eur. J.* **2021**, *27*, 4070–4080. https://doi.org/https://doi.org/10.1002/chem.202003916.

(30) Helten, H. Doping the Backbone of π-Conjugated Polymers with Tricoordinate Boron: Synthetic Strategies and Emerging Applications. *Chem. – An Asian J.* **2019**, *14*, 919–935. https://doi.org/https://doi.org/10.1002/asia.201900016.

(31) Yan, H.; Chen, J.; Zhou, K.; Tang, Y.; Meng, X.; Xu, X.; Ma, W. Lewis Acid Doping Induced Synergistic Effects on Electronic and Morphological Structure for Donor and Acceptor in Polymer Solar Cells. *Adv. Energy Mater.* **2018**, *8*, 1703672. https://doi.org/https://doi.org/10.1002/aenm.201703672.

(32) Marqués, P. S.; Londi, G.; Yurash, B.; Nguyen, T.-Q.; Barlow, S.; Marder, S. R.; Beljonne, D. Understanding How Lewis Acids Dope Organic Semiconductors: A “Complex” Story. *Chem. Sci.* **2021**, *12*, 7012–7022. https://doi.org/10.1039/D1SC01268A.

(33) Panidi, J.; Paterson, A. F.; Khim, D.; Fei, Z.; Han, Y.; Tsetseris, L.; Vourlias, G.; Patsalas, P. A.; Heeney, M.; Anthopoulos, T. D. Remarkable Enhancement of the Hole Mobility in Several Organic Small-Molecules, Polymers, and Small-Molecule:Polymer Blend Transistors by Simple Admixing of the Lewis Acid p-Dopant $B(C_6F_5)_3$. *Adv. Sci.* **2018**, *5*, 1700290. https://doi.org/https://doi.org/10.1002/advs.201700290.

(34) Han, J.; Ganley, C.; Hu, Q.; Zhao, X.; Clancy, P.; Russell, T. P.; Katz, H. E. Using Preformed Meisenheimer Complexes as Dopants for N-Type Organic Thermoelectrics with High Seebeck Coefficients and Power Factors. *Adv. Funct. Mater.* **2021**, *31*, 2010567. https://doi.org/https://doi.org/10.1002/adfm.202010567.

(35) Hubig, S. M.; Kochi, J. K. Direct Observation of the Wheland Intermediate in Electrophilic Aromatic Substitution. Reversible Formation of Nitrosoarenium Cations. *J. Am. Chem. Soc.* **2000**, *122*, 8279–8288. https://doi.org/10.1021/ja001318u.

(36) Hadzic, M.; Braïda, B.; Volatron, F. Wheland Intermediates: An Ab Initio Valence Bond Study. *Org. Lett.* **2011**, *13*, 1960–1963. https://doi.org/10.1021/ol200327s.

(37) Blasco, T. Identification of Wheland-Type Intermediates. *Nat. Catal.* **2018**, *1*, 8–9. https://doi.org/10.1038/s41929-017-0012-2.

(38) Reed, J. L. Hard and Soft Acids and Bases: Structure and Process. *J. Phys. Chem. A* **2012**, *116*, 7147–7153. https://doi.org/10.1021/jp301812j.

(39) Jursic, B. S. Calculation of Ionization Energy of Alkyl Radicals by Hybrid Density Functional Theory Methods. *J. Mol. Struct. THEOCHEM* **1998**, *432*, 211–217. https://doi.org/https://doi.org/10.1016/S0166-1280(98)00084-0.

(40) Liu, J.; Liu, W.; Aydin, E.; Harrison, G. T.; Isikgor, F. H.; Yang, X.; Subbiah, A. S.; De Wolf, S. Lewis-Acid Doping of Triphenylamine-Based Hole Transport Materials Improves the Performance and Stability of Perovskite Solar Cells. *ACS Appl. Mater. Interfaces.* **2020**, *12*, 23874-23884. https://doi.org/10.1021/acsami.0c03660.

(41) Zapata-Arteaga, O.; Perevedentsev, A.; Marina, S.; Martin, J.; Reparaz, J. S.; Campoy-Quiles, M. Reduction of the Lattice Thermal Conductivity of Polymer Semiconductors by Molecular Doping. *ACS Energy Lett.* **2020**, *5*, 2972–2978. https://doi.org/10.1021/acsenergylett.0c01410.

(42) Mateeva, N.; Niculescu, H.; Schlenoff, J.; Testardi, L. R. Correlation of Seebeck Coefficient and Electric Conductivity in Polyaniline and Polypyrrole. *J. Appl. Phys.* **1998**, *83*, 3111–3117. https://doi.org/10.1063/1.367119.

(43) Li, H.; Plunkett, E.; Cai, Z.; Qiu, B.; Wei, T.; Chen, H.; Thon, S. M.; Reich, D. H.; Chen, L.; Katz, H. E. Dopant-Dependent Increase in Seebeck Coefficient and Electrical Conductivity in Blended Polymers with Offset Carrier Energies. *Adv. Electron. Mater.* **2019**, *5*, 1800618. https://doi.org/https://doi.org/10.1002/aelm.201800618.

(44) Zuo, G.; Liu, X.; Fahlman, M.; Kemerink, M. High Seebeck Coefficient in Mixtures of Conjugated Polymers. *Adv. Funct. Mater.* **2018**, *28*, 1703280. https://doi.org/https://doi.org/10.1002/adfm.201703280.

(45) Lu, N.; Li, L.; Liu, M. A Review of Carrier Thermoelectric-Transport Theory in Organic Semiconductors. *Phys. Chem. Chem. Phys.* **2016**, *18*, 19503–19525. https://doi.org/10.1039/C6CP02830F.

(46) Shi, X.; Lu, N.; Xu, G.; Cao, J.; Han, Z.; Yang, G.; Li, L.; Liu, M. An Analytical Seebeck Coefficient Model for Disordered Organic Semiconductors. *Phys. Lett. A* **2017**, *381*, 3441–3444. https://doi.org/https://doi.org/10.1016/j.physleta.2017.09.006.

(47) He, M.; Qiu, F.; Lin, Z. Towards High-Performance Polymer-Based Thermoelectric Materials. *Energy Environ. Sci.* **2013**, *6*, 1352–1361. https://doi.org/10.1039/C3EE24193A.

(48) Upadhyaya, M.; Boyle, C. J.; Venkataraman, D.; Aksamija, Z. Effects of Disorder on Thermoelectric Properties of Semiconducting Polymers. *Sci. Rep.* **2019**, *9*, 5820. https://doi.org/10.1038/s41598-019-42265-z.

(49) Tanaka, H.; Kanahashi, K.; Takekoshi, N.; Mada, H.; Ito, H.; Shimoi, Y.; Ohta, H.; Takenobu, T. Thermoelectric Properties of a Semicrystalline Polymer Doped beyond the Insulator-to-Metal Transition by Electrolyte Gating. *Sci. Adv.* **2020**, *6*, 8065. https://doi.org/10.1126/sciadv.aay8065.

(50) Petrowsky, M.; Frech, R. Application of the Compensated Arrhenius Formalism to Self-Diffusion: Implications for Ionic Conductivity and Dielectric Relaxation. *J. Phys. Chem. B* **2010**, *114*, 8600–8605. https://doi.org/10.1021/jp1020142.

(51) Xu, Y.; Wang, X.; Zhou, J.; Song, B.; Jiang, Z.; Lee, E. M. Y.; Huberman, S.; Gleason, K. K.; Chen, G. Molecular Engineered Conjugated Polymer with High Thermal Conductivity. *Sci. Adv.* **2018**, *4*, 3031. https://doi.org/10.1126/sciadv.aar3031.

(52) Youngblood, G. E.; Thomsen, E. C.; Henager, C. H. Effects of Contact Resistance on Electrical Conductivity Measurements of SiC-Based Materials. *J. Nucl. Mater.* **2013**, *442*, 410–413. https://doi.org/https://doi.org/10.1016/j.jnucmat.2013.04.096.

(53) Lam, L.; Swingler, J.; McBride, J. The Contact Resistance Force Relationship of an Intrinsically Conducting Polymer Interface. In *Proceedings of the 50th IEEE Holm Conference on Electrical Contacts and the 22nd International Conference on Electrical Contacts Electrical Contacts, 2004.*; 2004; 304–311. https://doi.org/10.1109/HOLM.2004.1353134.

(54) Wang, R.; Guo, Y.; Zhang, D.; Zhou, H.; Zhao, D.; Zhang, Y. Improved Electron Transport with Reduced Contact Resistance in N-Doped Polymer Field-Effect Transistors with a Dimeric Dopant. *Macromol. Rapid Commun.* **2018**, *39*, 1700726. https://doi.org/https://doi.org/10.1002/marc.201700726.

(55) Prodanović, N.; Vukmirović, N. Charge Carrier Mobility in Systems with Local Electron-Phonon Interaction. *Phys. Rev. B* **2019**, *99*, 104304. https://doi.org/10.1103/PhysRevB.99.104304.

(56) Emin, D. Phonon-Assisted Jump Rate in Noncrystalline Solids. *Phys. Rev. Lett.* **1974**, *32*, 303–307. https://doi.org/10.1103/PhysRevLett.32.303.

(57) Li, L.; Van Winckel, S.; Genoe, J.; Heremans, P. Electric Field-Dependent Charge Transport in Organic Semiconductors. *Appl. Phys. Lett.* **2009**, *95*, 153301. https://doi.org/10.1063/1.3246160.

(58) Celle, C.; Suspène, C.; Ternisien, M.; Lenfant, S.; Guérin, D.; Smaali, K.; Lmimouni, K.; Simonato, J. P.; Vuillaume, D. Interface Dipole: Effects on Threshold Voltage and Mobility for Both Amorphous and Poly-Crystalline Organic Field Effect Transistors. *Org. Electron.* **2014**, *15*, 729–737. https://doi.org/https://doi.org/10.1016/j.orgel.2014.01.003.

(59) Jang, H.-J.; Wagner, J.; Li, H.; Zhang, Q.; Mukhopadhyaya, T.; Katz, H. E. Analytical Platform To Characterize Dopant Solution Concentrations, Charge Carrier Densities in Films and Interfaces, and Physical Diffusion in Polymers Utilizing Remote Field-Effect Transistors. *J. Am. Chem. Soc.* **2019**, *141*, 4861–4869. https://doi.org/10.1021/jacs.8b13026.

(60) Bachmann, M.; Czerner, M.; Heiliger, C. Ineffectiveness of Energy Filtering at Grain Boundaries for Thermoelectric Materials. *Phys. Rev. B* **2012**, *86*, 115320.

https://doi.org/10.1103/PhysRevB.86.115320.

(61) Lin, Y.; Wood, M.; Imasato, K.; Kuo, J. J.; Lam, D.; Mortazavi, A. N.; Slade, T. J.; Hodge, S. A.; Xi, K.; Kanatzidis, M. G.; Clarke, D. R.; Hersam, M. C.; Snyder, C. J. Expression of Interfacial Seebeck Coefficient through Grain Boundary Engineering with Multi-Layer Graphene Nanoplatelets. *Energy Environ. Sci.* **2020**, *13*, 4114–4121. https://doi.org/10.1039/D0EE02490B.

(62) Hermanek, S. Boron-11 NMR Spectra of Boranes, Main-Group Heteroboranes, and Substituted Derivatives. Factors Influencing Chemical Shifts of Skeletal Atoms. *Chem. Rev.* **1992**, *92*, 325–362. https://doi.org/10.1021/cr00010a007.

(63) Neese, F. The ORCA Program System. *WIREs Comput. Mol. Sci.* **2012**, *2*, 73–78. https://doi.org/https://doi.org/10.1002/wcms.81.

(64) Neese, F. Software Update: The ORCA Program System, Version 4.0. *WIREs Comput. Mol. Sci.* **2018**, *8*, 1327. https://doi.org/https://doi.org/10.1002/wcms.1327.

(65) Xu, B.; Yi, X.; Huang, T.-Y.; Zheng, Z.; Zhang, J.; Salehi, A.; Coropceanu, V.; Ho, C. H. Y.; Marder, S. R.; Toney, M. F.; Bredas; J.-L.; So, F.; Reynolds, J. R. Donor Conjugated Polymers with Polar Side Chain Groups: The Role of Dielectric Constant and Energetic Disorder on Photovoltaic Performance. *Adv. Funct. Mater.* **2018**, *28*, 1803418. https://doi.org/https://doi.org/10.1002/adfm.201803418.

(66) Sami, S.; Alessandri, R.; Broer, R.; Havenith, R. W. A. How Ethylene Glycol Chains Enhance the Dielectric Constant of Organic Semiconductors: Molecular Origin and Frequency Dependence. *ACS Appl. Mater. Interfaces* **2020**, *12*, 17783–17789. https://doi.org/10.1021/acsami.0c01417.

(67) Matheson, A. B.; Ruseckas, A.; Pearson, S. J.; Samuel, I. D. W. Hole Delocalization as a Driving Force for Charge Pair Dissociation in Organic Photovoltaics. *Mater. Horiz.* **2019**, *6*, 1050–1056. https://doi.org/10.1039/C8MH01204K.

(68) Gregg, B. A. Entropy of Charge Separation in Organic Photovoltaic Cells: The Benefit of Higher Dimensionality. *J. Phys. Chem. Lett.* **2011**, *2*, 3013–3015. https://doi.org/10.1021/jz2012403.

TOC Graphic

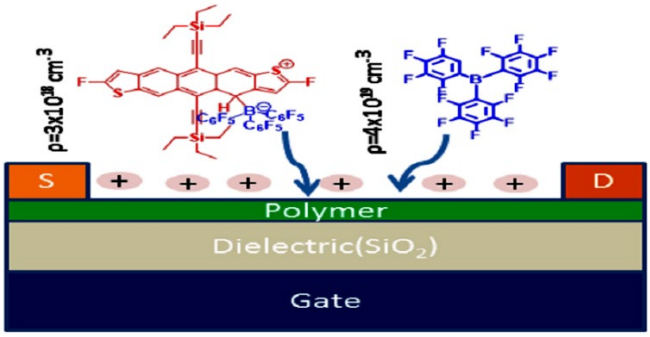

Remote Gate sensing